J. Fluid Mech. (2024), *vol*. 991, A9, doi:10.1017/jfm.2024.504

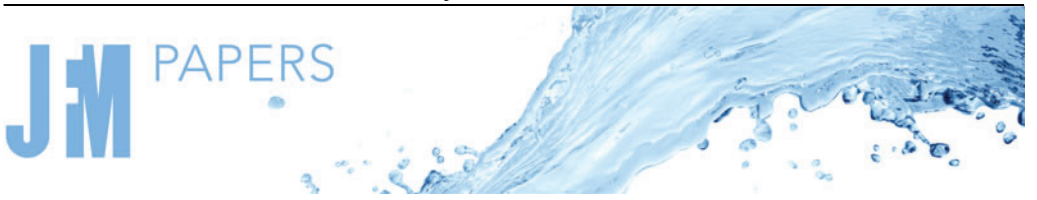

Low-frequency unsteadiness mechanisms of unstart flow in an inlet with rectangular-to-elliptical shape transition under off-design condition at a Mach number of 4

Jiaxiang Zhong[1], **Feng Qu**[1],†, **Di Sun**[1], **Qingsong Liu**[1], **Qing Wang**[1] and **Junqiang Bai**[1]

[1]School of Aeronautics, Northwestern Polytechnical University, Xi'an 710072, PR China

(Received 8 December 2023; revised 9 April 2024; accepted 19 May 2024)

The unsteady mechanism of unstart flow for an inlet with rectangular-to-elliptical shape transition (REST) under the off-design condition at a Mach of 4 is investigated using the delay detached eddy simulation method. With the help of numerical simulations, the unsteady dynamics, especially the low-frequency characteristics of the REST inlet unstart flow, as well as the self-sustaining mechanism, is investigated. The instantaneous flow illustrates the unsteady phenomena of the REST unstart flow, including the interaction between the cowl-closure leading edge (CLE) shock and the shear layer, breathing of the separation bubble, flapping of the separation shock, instability of the shear layer and vortex shedding along the shear layer. The spectral analysis reveals that the lower frequency dynamics is associated with the breathing of the separation bubble and the flapping motion of the separation shock wave, while the higher frequency is related to the instability of the shear layer affected by cowl-closure leading edge shock and the formation of shedding vortices. Further, coherence analysis shows that the contribution of these flow structures dominating the low-frequency dynamics couple with each other. Based on the dynamic mode decomposition results, the characteristics that contribute to the unsteady behaviour of unstart flow are summarized. The streamwise vortices downstream of the separation and the shedding vortices are believed to be the main driving force of the global low-frequency unsteadiness of the REST inlet unstart flow under the off-design condition. Moreover, the CLE shock plays an important role in the process during the dominant flow structure conversion from the backflow within the separation bubble into elongated streamwise structures.

Key words: boundary layer separation, shock waves, supersonic flow

† Email address for correspondence: qufeng@nwpu.edu.cn

1. Introduction

Since being proposed in 1940s, the scramjet has become the heart of the air breath propulsion system for the air breath hypersonic vehicle (Segal 2009). In a scramjet, the hypersonic inlet is an important component that compresses the incoming flow and provides it to the combustion chamber with suitable pressure and velocity. However, due to the immature design technique, as well as the discrepancy between the ground experiment conditions and the actual flight conditions and inlet unstart is inevitable in an operating hypersonic inlet (Tan, Sun & Yin 2009). The inlet unstart may not only bring structural damage to the inlet and the engine (Voland *et al.* 1999; Zheng, Yan & Zhao 2020; Bagheri *et al.* 2021), but also make the combustion chamber work abnormally and even flameout (Zheng *et al.* 2020; Sethuraman, Kim & Kim 2021). Over the past decades, many flight test failures were ascribed to the inlet unstart, including the NASA flight test (Rodriguez 2003) and the X-51A flight tests (Lewis 2010).

For this, the hypersonic inlet unstart has been widely investigated numerically and experimentally in the last decades, and there have been some detailed reviews on the characteristics and mechanisms of the unstart flow (Chang *et al.* 2017; Im & Do 2018). In general, inlet unstart is considered to be the result of multiple factors including the internal contraction ratio (ICR) (Sakata *et al.* 1993; Devaraj *et al.* 2021), backpressure (Tan *et al.* 2011; Chen & Tan 2019) and the local Mach number (Yuan & Liang 2006; Hillier 2007). For ICR-induced inlet unstart, Devaraj *et al*. investigated the local unstart of a hypersonic inlet at Mach 6 using proper orthogonal decomposition and dynamic mode decomposition (DMD) for a better understanding of the unstart phenomenon (Devaraj *et al.* 2021). Another research about ICR-induced local unstart was carried out by Jin *et al*., they experimentally studied the high-frequency and broadband-frequency characteristics of the oscillation in unstart flow caused by a large ICR (Jin *et al.* 2022). For the inlet of a turbine-based combined-cycle engine, Li *et al*. investigated its restart/unstart characteristics in detail and summarized the influences of the mode transition and backpressure on the hysteresis behaviour (Li *et al.* 2018). Yu experimentally studied the inlet unstart under different Mach numbers and successfully captured the typical flow structures of inlet start/unstart flows (Yu *et al.* 2018). Also, Tan et al. first discussed the oscillating flow caused by the downstream mass flow chocking by experiment at a Mach number of 5. The results indicated that unstart will make inlet performance reduce abruptly due to the shock wave system oscillations and the prominent pressure fluctuations. Further, they classified the oscillatory unstart flows into two types, which are ‘little buzz’ and ‘big buzz’ (Tan *et al.* 2009). Owing to the researchers’ efforts, the unstart mechanism of a two-dimensional inlet and sidewall compression inlet is considered to be well understood. However, the three-dimensional inward-turning inlet, which consists of complex compression surfaces leading to more complex flow structures and phenomena, still poses great challenges for its application.

In comparison with the canonical hypersonic inlet, the three-dimensional inward-turning inlet with a cross-sectional shape transition to an elliptical throat is more feasible to be used in combination with an elliptical combustor. It is superior to a rectangular cross-section in terms of the structural weight required to support a specified pressure and the wetted area needed to enclose a specified flow area (Smart 1999). Correspondingly, the rectangular-to-elliptical shape transition (REST) gives the inlet a large ICR and wetted area. In practice, the inlet in a combined-cycle engine should operate under the off-design condition before being accelerated to the cruise point. Operating at such a low Mach number, especially for the REST inlet with a large ICR, will lead to inlet unstart in all probability and even result in engine flameout (Tan *et al.* 2009). More importantly, for

an accelerating scramjet that must operate at high Mach numbers, the mode transitions must be accomplished smoothly, and the impacts on the overall acceleration of the engine should be minimized (Rohde 1992). However, most of the efforts for previous studies are concentrated on the mechanism under the design point of the inlet, only a few of them are put into the unstart flow under the off-design condition. Smart and Trexler investigated the start performance of a REST inlet under the off-design condition at a Mach number below its design point by experiment (Smart & Trexler 2004). Their study revealed that the REST inlet is a viable configuration for vehicles operating over a wide Mach number range, but the inlet will fall into unstart at off-design conditions without appropriate boundary-layer conditioning. Zveginstsev also proved that the flow in the engine duct becomes extremely complicated in off-design modes of inlet operation, which can lead to unpredictable consequences, in particular, to inlet unstart (Zvegintsev 2017). Li *et al*. proposed a tomography-like flow visualization and realized the sliced visualization of the internal flow of the REST inlet (Yiming, Zhufei & Zhang 2021). However, it is still unable to achieve experimental study well for the microscopic flow structure and the interferences between flow structures. Liu *et al*. and Yu *et al*., respectively, investigated the hypersonic internal flow under off-design conditions and the basic characteristics of the unstart flow are summarized (Liu, Liang & Wang 2016; Yu *et al.* 2018). Furthermore, Johnson *et al*. studied the inlet designed for Mach 5.5 based on the stream-tracing technology at the off-design condition at Mach 4 (Johnson *et al.* 2023). Their results are the same as those of Smart (Smart & Trexler 2004); the inlet could not start without any flow control strategies. Therefore, the inlet unstart phenomenon under off-design conditions should be considered and more efforts are required to understand the mechanism of the REST inlet unstart flow, especially the transitional condition.

From previous studies, the REST inlet unstart flow under the transitional condition, i.e. a specific off-design condition, is a typical self-sustained shock wave–boundary-layer interaction (SWBLI) system with significant low-frequency unsteady features (Li *et al.* 2017). In terms of the low-frequency unsteady mechanisms of SWBLI systems, considerable studies were carried out in the canonical two-dimensional SWBLI configurations, including the incident (impinging–reflecting) shock (Ganapathisubramani, Clemens & Dolling 2007), compression ramp (Grilli, Hickel & Adams 2013; Pasquariello, Hickel & Adams 2017) and backward-facing step (BFS) and forward-facing step (Hu, Hickel & Van Oudheusden 2019, 2020, 2021). In all the cases, the SWBLI is accompanied by unsteady motions at frequencies that are one or two orders lower than the boundary-layer characteristic frequency (Touber & Sandham 2009, 2011). Therefore, tracing the source of this low-frequency unsteadiness is of particular interest. For the two-dimensional inlet and sidewall compression inlet, the SWBLI within these configurations can be simplified into canonical two-dimensional SWBLI cases and their unsteady mechanism is to be well understood. However, the complex flow structures, a series of shock waves, expansion and vortices within the internal flow of the REST inlet, still pose great challenges for the unsteady mechanism explosion of the REST inlet unstart flow. In the current study, we tend to investigate the low-frequency unsteady mechanism in the unstart flow on the REST inlet under its off-design condition. It is beneficial to the better understanding of the inlet unstart phenomenon and helps the design of flow control strategies and the development of an integrated design technology for the REST inlet with a forebody. Moreover, the investigation of the low-frequency unsteadiness mechanism of the REST inlet is also a good supplement to the current SWBLI theories. In this study, the unstart phenomenon of a hypersonic inlet with REST under the off-design operating condition is numerically studied by adopting delay detached eddy simulation (DDES).

The unsteady dynamics, especially the low-frequency characteristic of the REST inlet unstart flow, as well as the self-sustaining mechanism of the unstart flow, are investigated. By comparing with the canonical SWBLI configurations, the differences and connections between the low-frequency unsteadiness characteristics in the REST inlet unstart flow and the canonical configurations, and the internal flow mechanism of the inlet unstart flow, are presented. The key conclusions of these unsteady flow phenomena are promising to help a better understanding of the REST inlet unstart and guide the design of effective unstart flow control methods.

The organization of the paper is as follows. The numerical method and detailed computational set-up are given in § 2. Thereafter, the flow patterns of the mean flow and instantaneous flow are summarized in § 3. Also, the characteristic frequencies of the significant unsteady motion are analysed using spectral analysis and the dominating modes in the unstart flow are extracted via three-dimensional DMD. Finally, to characterize the low-frequency evolution of the unstart flow, a physical mechanism of the unsteady REST inlet unstart flow is proposed in § 4. The conclusions of the main results are presented in § 5.

2. Methodology

2.1. *Delay detached eddy simulation*

The basic governing equations are the Reynolds-averaged Navier–Stokes (RANS) equations. For the additional Reynolds stress in the RANS equations, researchers have constructed many turbulence models to solve it. The shear-stress transport (SST) turbulence model proposed by Menter (1994) is adopted in the current study.

The two-equation SST DDES method is implemented by modifying the dissipation-rate term of the turbulent kinetic energy transport equation as follows:

$$\frac{\partial(\rho k)}{\partial t}+\frac{\partial\left(\rho U_i k\right)}{\partial x_i}=\tilde{P}_k-\frac{\rho k^{3/2}}{l_{hybrid}}+\frac{\partial}{\partial x_i}\left[\left(\mu+\sigma_k\mu_t\right)\frac{\partial k}{\partial x_i}\right], \tag{2.1}$$

$$\frac{\partial(\rho\omega)}{\partial t}+\frac{\partial\left(\rho U_i k\right)}{\partial x_i}=\frac{\gamma}{v_t}\tilde{P}_k-\beta\rho\omega^2+\frac{\partial}{\partial x_i}\left[\left(\mu+\sigma_\omega\mu_t\right)\frac{\partial\omega}{\partial x_i}\right]+2\left(1-F_1\right)\rho\frac{\sigma_{\omega 2}}{\omega}\frac{\partial k}{\partial x_i}\frac{\partial\omega}{\partial x_i}, \tag{2.2}$$

where ρ is the density, μ is the viscosity, γ is the specific heat ratio, σ_k and σ_w are diffusion coefficients of k and ω, P_k is the production term of turbulent kinetic energy, k and ω represent the turbulent kinetic energy and specific dissipation rate, respectively, β is a constant and its value is recommended as 0.09 by Menter (1994). Additionally, l_{hybrid} is the length scale and is defined as

$$l_{hybrid}=\min\left\{l_{RANS}, l_{LES}\right\}, \tag{2.3}$$

$$l_{RANS}=\frac{k^{1/2}}{\beta\omega},\quad l_{LES}=C_{DES}\Delta=C_{DES}\max\left\{\Delta_x, \Delta_y, \Delta_z\right\}, \tag{2.4a,b}$$

where l_{RANS} and l_{LES} are the length scales of the RANS turbulence model and the large eddy simulation (LES) method. Here, δ is the grid scale, which is equal to the maximum grid spacing in the x, y and z directions for the structured grid and C_{DES} is an empirical constant that needs to be calibrated and verified, reflecting the degree of dissipation in different computational fluid dynamics codes. For the SST turbulence model, $C_{DES}=(1-F_1)C_{DES}^{outer}+F_1C_{DES}^{inner}$, where $C_{DES}^{outer}=0.61$, $C_{DES}^{inner}=0.78$ and F_1 is the internal function in the SST turbulence model (Spalart *et al.* 2006).

Furthermore, within the DES method exists modelled-stress depletion, which will produce the grid-induced separation. For this, Spalart *et al*. proposed a new method, named DDES, by constructing a delayed function (Spalart *et al.* 2006). The length scale of DDES can be expressed as follows:

$$\left.\begin{aligned} l_{hybrid} &= l_{RANS} - f_d \max\{0, l_{RANS} - l_{LES}\} \\ f_d &= 1 - \tanh\left[(8r_d)^3\right] \\ r_d &= \frac{v + v_t}{\sqrt{u_{i,j}u_{i,j}}\kappa^2 d^2} \end{aligned}\right\}, \tag{2.5}$$

where f_d is the delayed function, μ_t is the kinematic eddy viscosity, μ is the molecular viscosity, $u_{i,j}$ are the velocity gradients, κ is the Kármán constant of 0.41 and d is the distance to the wall. A more detailed introduction of the delayed function and the meaning of the parameters can be found in Spalart *et al.* (2006).

2.2. *Dynamic mode decomposition*

We follow the method of Rowley *et al.* (2009) and Schmid (2010) to perform DMD (also referred to as Koopman mode decomposition) of the three-dimensional flow field. We take $m + 1$ snapshots of three velocity components at each spatial location and express the last snapshot as a linear combination of the previous snapshots. The size of each x_i is the number of grid points multiplied by the number of velocity components. Let K represent a matrix of the different snapshots from x_0 to x_{m-1}

$$K = \left[x_0, x_1, x_2, \ldots, x_{m-1}\right]. \tag{2.6}$$

Suppose each snapshot (x_i) is obtained from the application of a linear matrix A to the previous snapshot (x_{i-1})

$$K = \left[x_0, Ax_0, A^2x_0, \ldots, A^{n-1}x_0\right]. \tag{2.7}$$

Now, expressing the last snapshot (x_m) as a linear combination of the previous snapshots

$$x_m = c_0x_0 + c_1x_1 + c_2x_2 + \cdots + c_{m-1}x_{m-1} + r = Kc + r. \tag{2.8}$$

In the above equation, r represents the residual of the linear combination. If the residual is zero, then the above representation would be exact. Here, C is given by

$$c = (c_0, c_1, c_2, \ldots, c_{m-1}). \tag{2.9}$$

The vector c is obtained by solving the least-squares problem in (2.6) using singular value decomposition. Based on the above definitions, we obtain

$$AK = KC + re^t, \quad e^t = (0, 0, \ldots, 1), \tag{2.10a,b}$$

where C is a companion matrix whose eigenvalues approximate those of the matrix A, which represents the dynamics of the flow. The imaginary part of the eigenvalue gives the frequency while the real part gives the growth rate of the mode. The eigenvector (ν) or the spatial variation of the DMD mode is obtained from the eigenvector of the companion matrix (C) and the matrix (K). The energy of each DMD mode is the $L2 - norm$ of the eigenvector ν. Here, the vectors x_i are obtained by the operation of the nonlinear Navier–Stokes operator and the eigenvalues and eigenvectors approximate the Koopman modes of the dynamical system. Further theoretical and implementation details can be obtained in Rowley *et al.* (2009) and Schmid (2010).

Mach number	Ma_∞	6.0
Angle of attack	α_∞	0
Static pressure (Pa)	P_∞	2549.2
Static temperature (K)	T_∞	221.55
Stagnation pressure (kPa)	$P_{0,\infty}$	4024.9
Stagnation temperature (K)	$T_{0,\infty}$	1816.71

Table 1. Flow conditions for the REST inlet at the design operating condition.

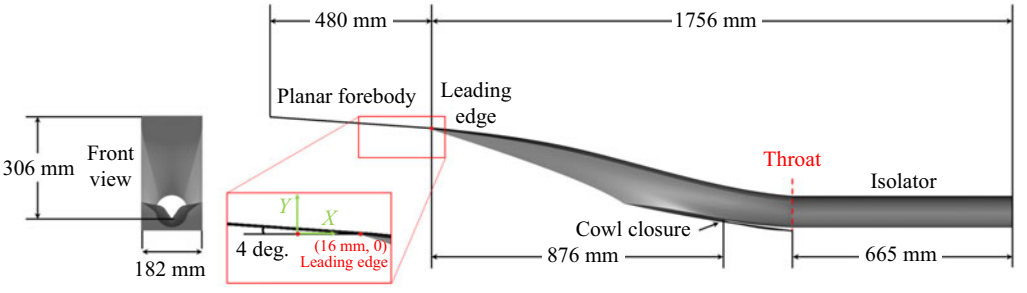

Figure 1. Side and front views of the REST inlet geometry.

2.3. *Model and grid*

The inlet model adopted in the current study is a typical REST inlet designed by a streamline tracing technology for hypersonic flight at a Mach of 6. The free-stream flow parameters in the design condition are shown in table 1. The surface geometry and detailed measurements are provided in figure 1. Also, the definition of the coordinate origin and axis system is marked in figure 1, in which the location of the inlet leading edge is (16 mm, 0). The model is a total of 1756 mm in length, measured from the leading edge of the compression surfaces to the aft of the isolator. The capture width is 75 mm, measured between the leading edge of each sidewall, and the capture height is 306 mm with a total geometric contraction ratio of 6.98 and an ICR of 1.25. The cowl closure occurs 876 mm downstream from the leading edge (80 % of compression surfaces' length). In addition, REST inlets are usually designed for a specific flight Mach number with an assumed forebody precompression. The current inlet is assumed to be integrated into a vehicle with a planar forebody with 4° of attack. Therefore, a planar forebody is located in front of the leading edge, which is 480 mm in length and with an angle of 4°.

Figure 2 displays the schematics of the computation domain and boundary conditions for the simulations, in which the grid is coarsened by a factor of 4 for clarity. A multi-block structured grid with 1.3×10^7 cells is utilized and the grids are refined near the leading edge and body wall. To ensure that the boundary layers, shock interactions and separation zones are resolved properly, the grid is refined in the near-wall region along the normal direction. The first grid spacing from the wall is chosen to ensure that $y+ < 1$. The grid blends smoothly from very high grid density around the leading edge and wall surfaces to coarser grid space in the free-stream region where the flow is smooth. During the simulation, all the outer boundaries are set to be far field, except for the exit planes, which have applied supersonic outflow. All the wall surfaces are no slip and the wall is adiabatic.

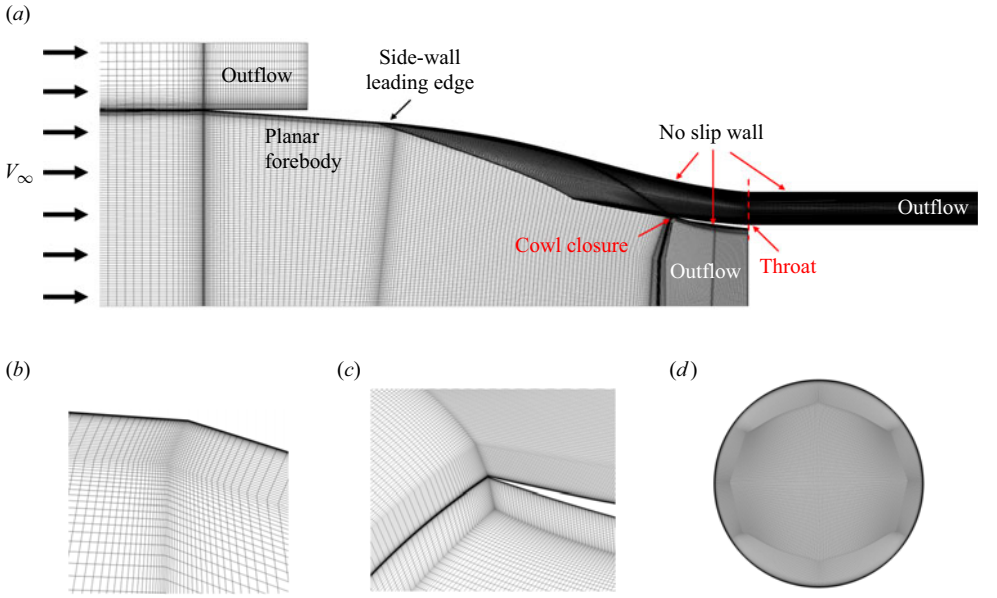

Figure 2. Sketch of inlet computational grid. (*a*) Overview of the grid. (*b*) Zoom-in view near the cowl-closure leading edge. (*c*) Zoom-in view near the sidewall leading edge. (*d*) Zoom-in view near the throat.

Mach number	Ma_∞	4.0
Angle of attack	α_∞	0
Static pressure (Pa)	P_∞	8849.73
Static temperature (K)	T_∞	216.65
Stagnation pressure (kPa)	$P_{0,\infty}$	1343.7
Stagnation temperature (K)	$T_{0,\infty}$	909.93

Table 2. Flow conditions for the REST inlet at the off-design operating condition.

2.4. *Computational details*

In this study, all the numerical simulations are performed by an in-house three-dimensional finite volume solver developed by the authors. This solver has been successfully applied to considerable numerical studies on both supersonic and hypersonic flows (Qu & Sun 2017; Sun, Qu & Yan 2018; Qu *et al.* 2019; Sun *et al.* 2021; Wang *et al.* 2022, 2023), in which it reasonably captured the complex shock structures and vortical flows. The code solves the three-dimensional compressible Navier–Stokes equations using the detached eddy simulation method coupled with the two-equation SST turbulence model. A Roe flux-difference upwind scheme with a fifth-order weighted essentially non-oscillatory scheme (Liu, Osher & Chan 1994) flux limiter is employed because of their low numerical dissipation and advantage in flow structure capturing, such as supersonic mixing layer flow, SWBLI region and so on. The state equation for an ideal gas is used, the molecular viscosity is assumed to obey Sutherland's law and the ratio of specific heat γ is 1.4. Detailed free-stream flow parameters at the transitional operating condition are provided in table 2.

In order to accelerate the evolution of the unsteady motions for unstart flow, all the DDES simulations are carried out based on the converged steady RANS solutions.

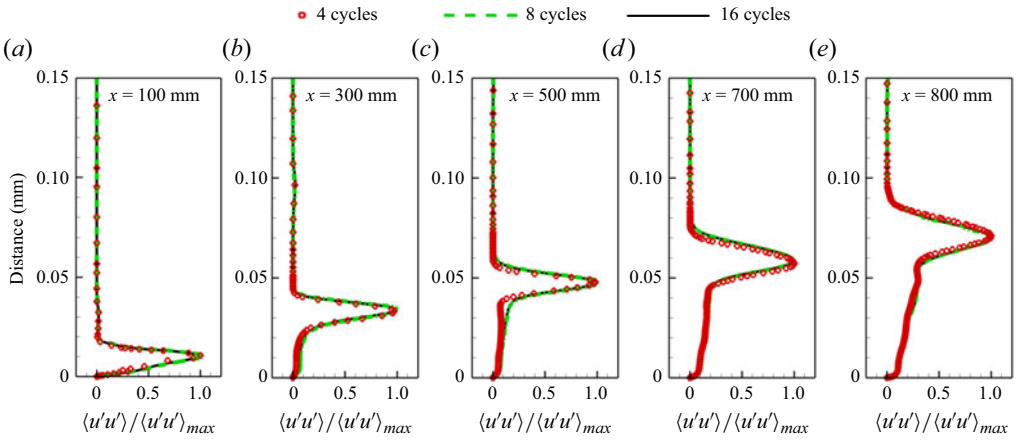

Figure 3. Root mean square of U velocity fluctuations in time-averaged flow obtained by different averaging periods.

Thereafter, the unsteady DDES simulations are performed and a fixed physical time step of 3×10^{-4} s is employed. In order to ensure the residual at each physical time step is reduced by at least 2–3 orders, 50 subiterations are used for each physical time step. The first 100 000 time steps (corresponding to a physical time period of 30 s) are used to obtain a basic unsteady flow. The subsequent 50 000 time steps (corresponding to a physical time period of 15 s), which contain roughly 16 cycles of the global motion, are employed to obtain the averaged flow and the instantaneous flows used in the following analyses. Figure 3 presents the time-averaged results of the root mean square of the U velocity fluctuation for specific probe positions obtained by different averaging periods (0–4, 0–8, 0–16). From figure 3, the time-averaged results obtained from 8 cycles and 16 cycles show excellent consistency, which is the same for the other parameters of the present simulation. Therefore, it can be considered that the simulation time for the current case is long enough and the effects of initial conditions are negligible.

2.5. *Code validation and grid sensitivity*

2.5.1. *Code validation*

In an operating hypersonic inlet, there are always intense SWBLIs and interactions between shock waves. Further, when the engine is operating over a wide range of conditions, the flow inside the inlet changes drastically, which makes the flow patterns more complex (Tan, Sun & Huang 2012; Qin *et al.* 2015; Xu *et al.* 2016; Li *et al.* 2017; Huang *et al.* 2018). Therefore, the solver is required to simulate the inlet flow with high accuracy around the SWBLI region.

To check the validity of the numerical method adopted in the current study, the solver is validated by comparing the numerical solution with the experimental result of a typical three-dimensional crossing shock interaction model in Kussoy & Horstman (1992). The validation model consists of two sharp fins fastened to a flat plate. The oblique shock waves, generated by the fins, intersect each other and interact with the flat plate turbulent boundary layer. Figures 4 and 5 display the geometric parameters, grid distribution and numerical set-up of the validation model. In the experiment, a weak oblique shock wave is induced by the boundary layer at the flat plate leading edge, causing a slight increase in the downstream wall pressure. To eliminate its effect, the free-stream parameters are

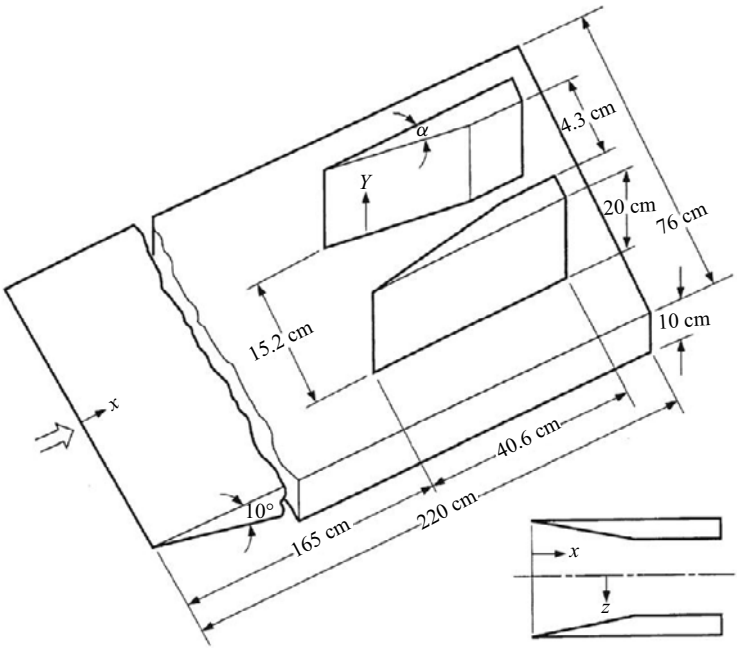

Figure 4. Geometric parameters and coordinate system of the validation model. The wedge angle for the double fins is $\alpha = 15^\circ$. The arrow indicates the free-stream flows from the leading of the flat plate toward the double fins. The leading edges of the flat plate and the double fins are sharp, and the model is symmetric to the plane $z = 0$ mm (Kussoy & Horstman 1992).

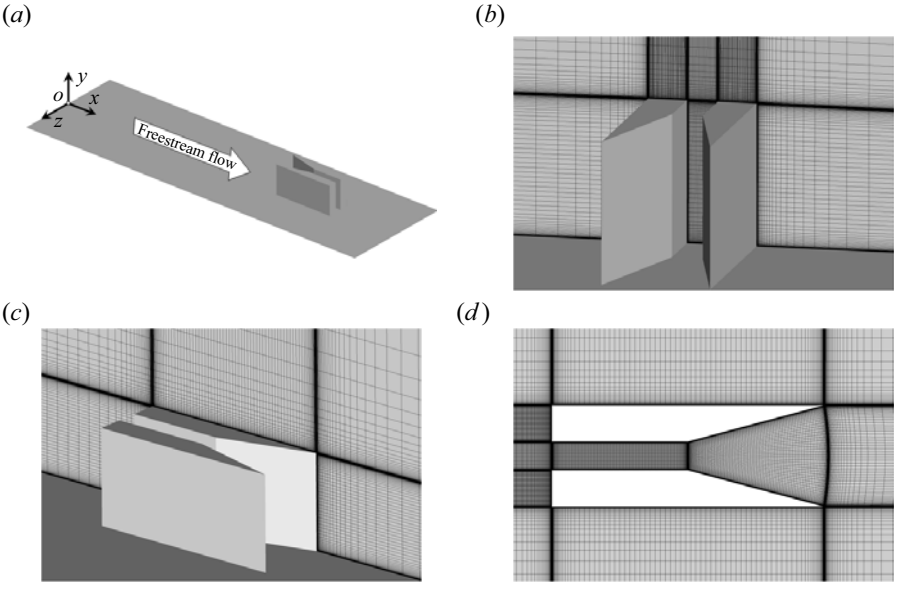

Figure 5. Sketch of the computational geometry and grid for the double-fin simulation. (*a*) Overview of the computational geometry. (*b–d*) Zoom-in views of the grid distributions.

Mach number	Ma_∞	8.23
Reynolds number	$Re_{\delta 0}$	1.7×10^5
Boundary-layer thickness (m)	δ_0	0.0325
Reference temperature (K)	T_∞	80
Stagnation temperature (K)	$T_{0,\infty}$	1177
Wall temperature (K)	T_w	300
Reference density (kg m^{-3})	ρ_∞	0.0186

Table 3. Free-stream flow parameters for double-fin simulation.

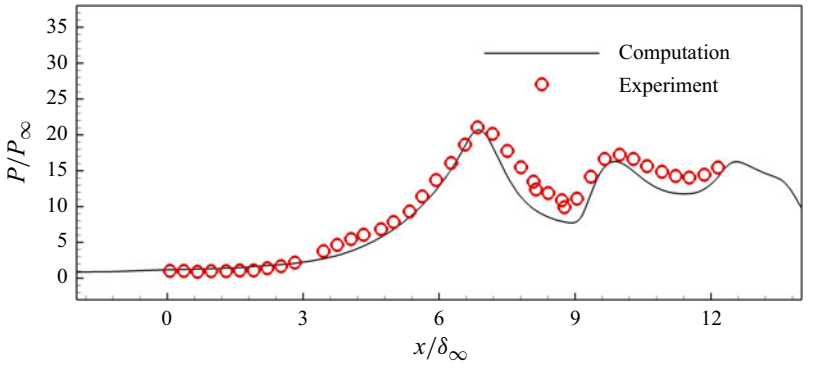

Figure 6. Experimental and computed wall pressure at the centre line of the double-fin configuration.

diagnosed at 3 cm ahead of the double fins, which has a Mach number $Ma_\infty = 8.23$ and Reynolds number $Re_{\delta 0} = 1.7 \times 10^5$ based on the local boundary-layer thickness $\delta_0 = 3.25$ cm. The other free-stream flow parameters are the same as the experimental set-up, as shown in table 3, and the numerical strategy is the same as that in § 2.4.

From all the computational results shown in figures 6 and 7, the comparison between the computed and experimental wall pressure distributions shows good agreement, indicating that the location and strength of the shock interactions and shock wave–boundary-layer interactions are well captured. Furthermore, the yaw angle is exported from the results, which is defined by $\tan^{-1}(w/u)$, where w and u are the velocities in the z (spanwise) and x (streamwise) directions, respectively, as shown in figure 8. The yaw angle represents the local direction of the velocity vector in a plane parallel to the flat plate. From figure 8, the computed yaw angle results show good agreement with the experimental values, indicating that the Flow structures are captured with high accuracy by the solver.

In addition to the double-fin configuration, another configuration with strong unsteady characteristics is adopted to verify the numerical method adopted in the current study. The configuration is an open backward-facing step (BFS) with a supersonic inflow (Hu *et al.* 2019, 2020, 2021), a sketch of which is shown in figure 9. The supersonic inflow is characterized by the free-stream Mach number $Ma_\infty = 1.7$ and the Reynolds number $Re_{\delta_0} = 13718$ based on the inlet boundary-layer thickness δ_0 and the free-stream values for velocity u_∞ and viscosity μ_∞. The detailed free-stream flow parameters are shown in table 4. The size of the computational domain corresponds to $[Lx, Ly, Lz] = [110\delta_0, 33\delta_0, 16\delta_0]$, including a length of $40\delta_0$ upstream of the step. The DDES simulation is conducted based on the converged steady RANS solution. Thereafter, a fixed time step

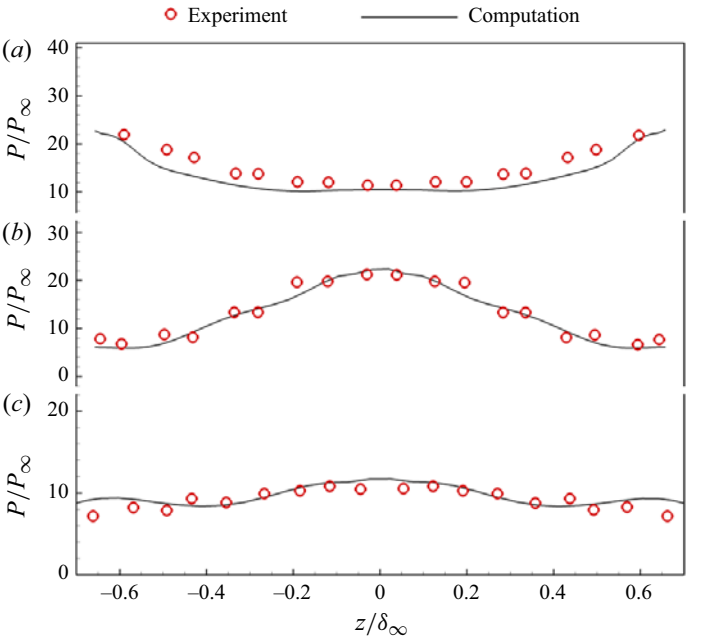

Figure 7. Experimental and computed wall pressure at (*a*) $x/\delta_\infty = 5.6$, (*b*) $x/\delta_\infty = 6.92$, (*c*) $x/\delta_\infty = 8.31$.

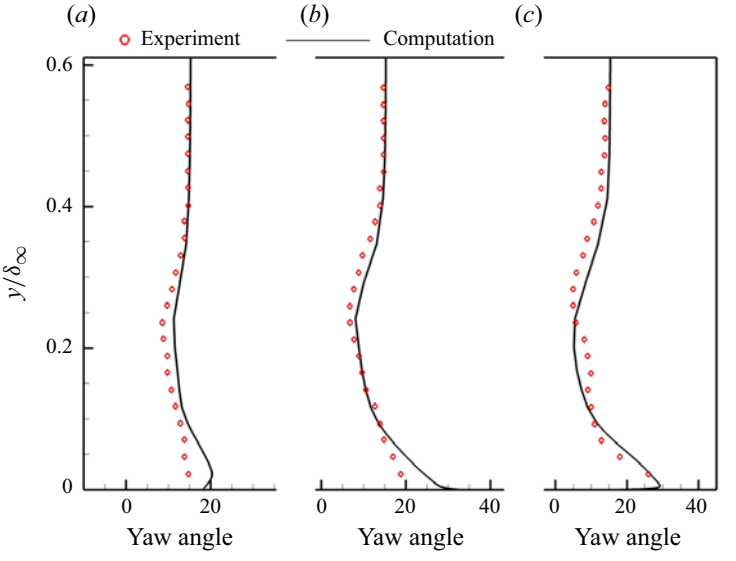

Figure 8. Experimental and computed yaw angle profiles at (*a*) $x/\delta_\infty = 5.6$, (*b*) $x/\delta_\infty = 6.92$, (*c*) $x/\delta_\infty = 8.31$.

of 3×10^{-7} s is used for the calculation, and 20 subiterations are required to ensure the residual at each physical time step reduces by at least two orders of magnitude. The first 40 000 time steps are employed to establish a statistically stationary state, and then statistics are gathered for the additional 10 000 time steps.

Figure 10 presents the comparison of the computed distribution and the reference values of the typical parameters along the centre line including the skin friction, the wall pressure and the root mean square of the wall pressure fluctuation. In addition, the U velocity profile

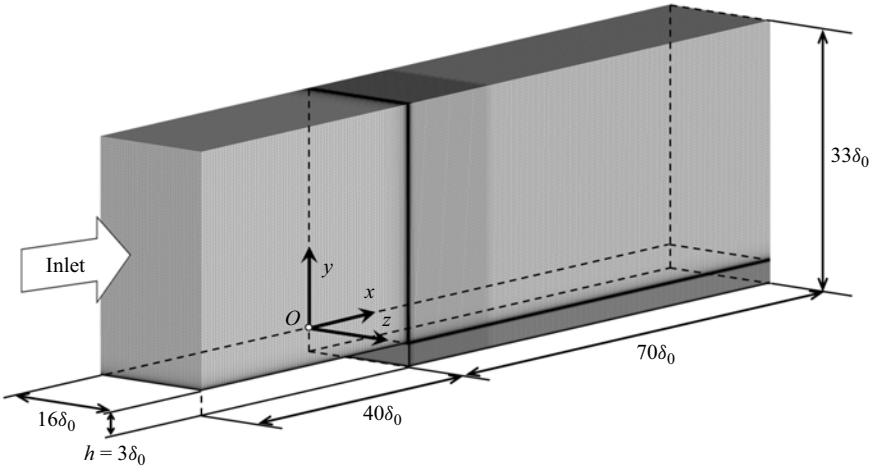

Figure 9. Sketch of the computational domains and grid for backward-facing step simulation.

Ma_∞	u_∞	δ_0	Re_∞	T_0	P_0	P_∞
1.7	469.85 m s^{-1}	1 mm	1.3718×10^7 m^{-1}	300 K	1×10^5 Pa	20 259 Pa

Table 4. Free-stream flow parameters for backward-facing step simulation.

of several positions is provided in figure 11. The results are in good agreement with the reference results. In the separated region and the shear layer, the solver utilized in the current study keeps high solution accuracy.

In summary of the validation cases, the numerical approach adopted in the present study appropriately describes the flow field including the incident shock, the reflected shock and the SWBLI region as well as the separation bubble.

2.5.2. *Grid sensitivity*

In the current study, two different mesh sizes were adopted to validate the grid independence of the solution. The coarse mesh contains a total of 9.6 *million* grids, and the fine mesh contains a total of 13.2 *million* grids. The diagrams of the computational meshes of the whole computational domain are provided in figure 2. To ensure an accurate solution in the boundary layer, SWBLI region and the separated region, the grids are refined near the wall and the region where complex flow structures are generated. The first grid spacing from the wall is set to ensure that $y+ < 1$.

Figure 12(*a*) displays the time-averaged flows for the slice at the throat for both the fine and coarse grids. Also, the U velocity profiles of specific probe points obtained by both two grids are provided in figure 12(*b*). From the results, the U velocity profiles and the flow fields obtained by the two meshes show good agreement and the two meshes demonstrate good grid independence. Furthermore, to obtain more convincing DDES results, the grid size should be small enough to resolve the desired turbulent structures. In the current study, the smallest Kolmogorov scale $\eta = (\nu^3/\epsilon)^{1/4}$ is estimated to be approximately 0.08 mm in the SWBLI region and the shear layer. Here, ν and ϵ are the kinematic viscosity, obtained according to Sutherland's law, and the turbulent kinetic energy dissipation rate,

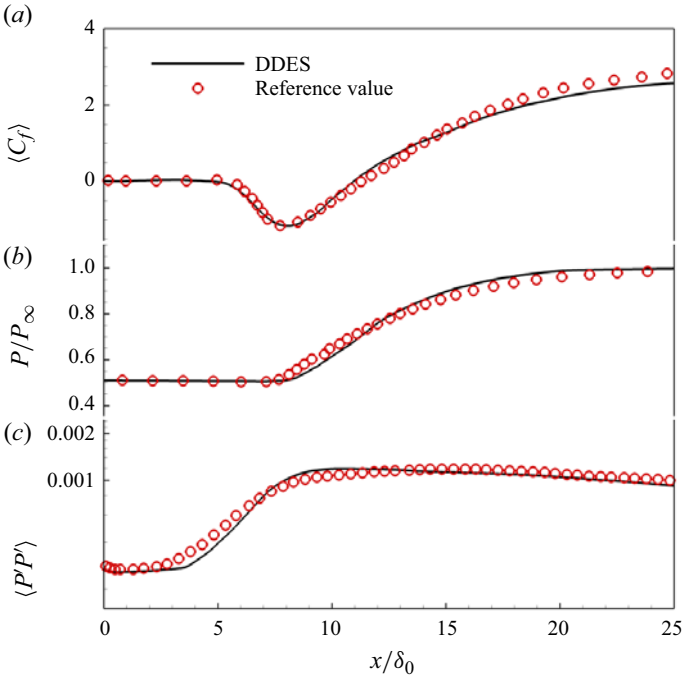

Figure 10. Experimental and computed results for BFS configuration of (*a*) skin friction, (*b*) wall pressure distribution and (*c*) root mean square of wall pressure fluctuation.

estimated by the re-normalization group (RNG) $k-\epsilon$ model. In the fine grid used in this study, the grid spacing around the SWBLI regions and the shear layer in (x, y, z) directions are specified to be $(1.0, 0.6, 0.5)$ mm, which are $(12.5, 7.5, 6.25)$ times the smallest Kolmogorov scale. In summary, the fine grid is considered to be fine enough to resolve the desired flow structures and will be adopted in the present investigations.

3. Results and discussion

3.1. *Mean flow features*

Figures 13 and 14 provide the overall view of the main flow topology of the averaged flow. With the free-stream flow passing the inlet leading edge, a ramp shock is generated by the planar forebody. After the planar forebody, a large-scale separation bubble is located on the compression wall. The overall profile of the bubble is visualized in figure 14 by the iso-surface of $u = 0$ and the maximum thickness of the bubble is $\delta_{max} = 46.5$ mm observed at $x = 736.5$ mm. The separation point is located at $x = 11.1$ mm ~ 30.0 mm and the separation shock wave is oriented at an angle of $\eta = 19.3^\circ \sim 20.2^\circ$. In other words, the separation point is more forward at the further spanwise position and the shock angle is smaller.

Figures 15 and 16 display the wall pressure distribution of the inlet model and specific sampling lines with different spanwise positions. Also, the selection of sampling lines is shown in figure 15. From the results, the pressure on the compression wall of different sampling lines shows more similarity compared with the lower wall. To ensure high-efficiency flow compression, the curvature of the compression wall is smaller, leading to a similar wall pressure distribution. At $x = 11.1$ mm ~ 30.0 mm, the flow experiences

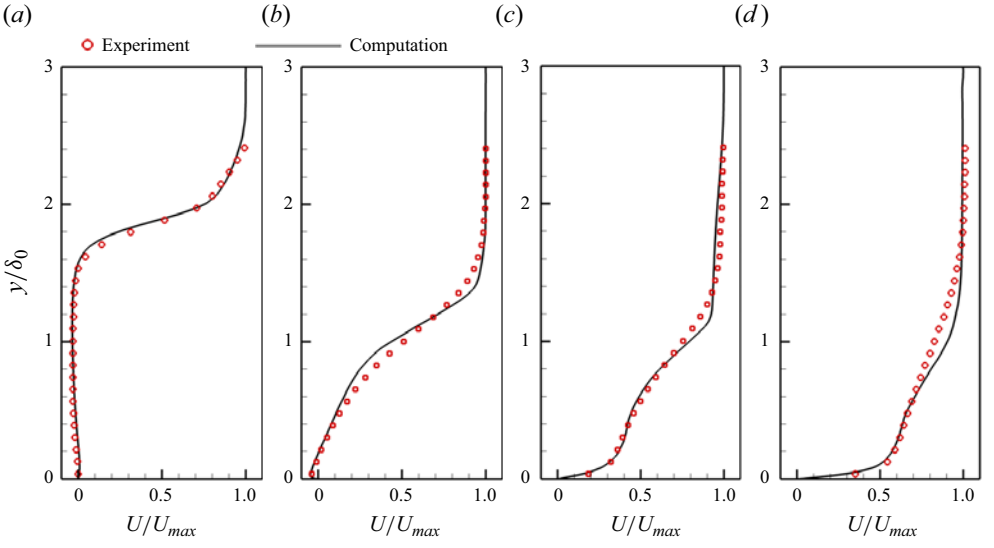

Figure 11. Experimental and computed U velocity profiles at (*a*) $x/\delta_0 = 5$, (*b*) $x/\delta_0 = 10$, (*c*) $x/\delta_0 = 15$, (*d*) $x/\delta_0 = 20$.

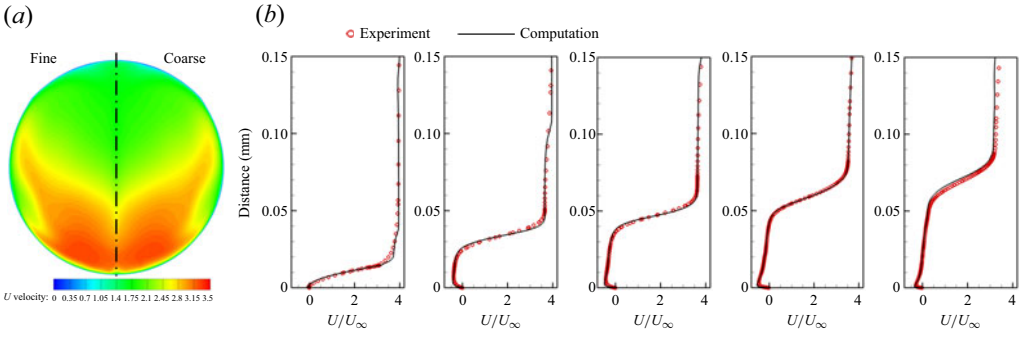

Figure 12. Time-averaged results obtained by coarse grid and fine grid; (*a*) U velocity contours at the throat, (*b*) U velocity profiles at probe the points; $x = 100$ mm, $x = 300$ mm, $x = 500$ mm, $x = 700$ mm, $x = 800$ mm.

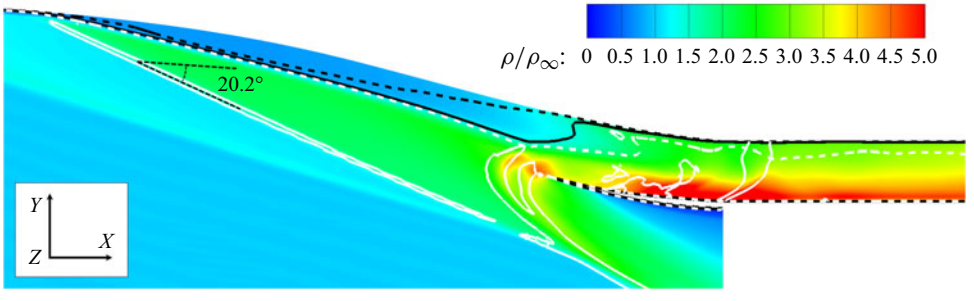

Figure 13. Density contours of the time- and spanwise-averaged flow field for slice $z = 0$. The white dashed and solid lines denote the isolines of $Ma = 1.0$ and $\partial P/\partial X = 25$. The black dashed and solid lines signify isolines of $u = 0$ and $u/u_\infty = 0.99$.

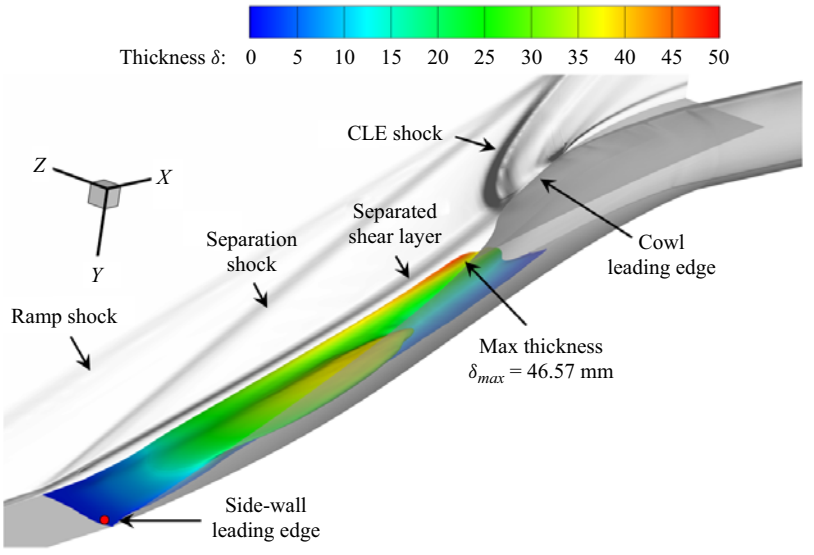

Figure 14. Separation bubble of time-averaged flow filed visualized by iso-surfaces of $u = 0$, coloured by the separation bubble thickness. A numerical schlieren at $z = 0$ slice is also included.

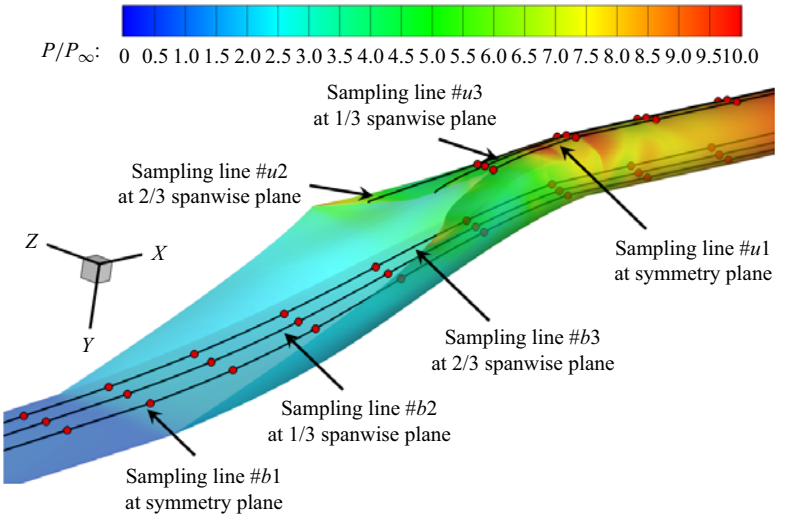

Figure 15. Wall pressure distribution and sampling lines of the time-averaged flow field on the upper (marked by #*u*) and bottom (marked by #*b*) walls. Pressure is normalized by the free-stream static pressure. The position of wall pressure probe points is indicated by the red dots.

a slight pressure increase on passing through the separation shock. At $x = 1105.1$ mm, an obvious pressure drop can be observed due to the expansive fan induced by the shape transition near the throat. Because of the expansive fan, the skin friction is lower near the throat compared with that of the region beside the throat.

After the throat, the pressure continuously increases under the influence of serious reflected shock waves. In contrast, the pressure distributions on the lower wall at different spanwise positions show clear differences because of the cowl leading edge with a large swept-back angle and the profile with large curvature. As shown in figure 16(*b*), a sharp

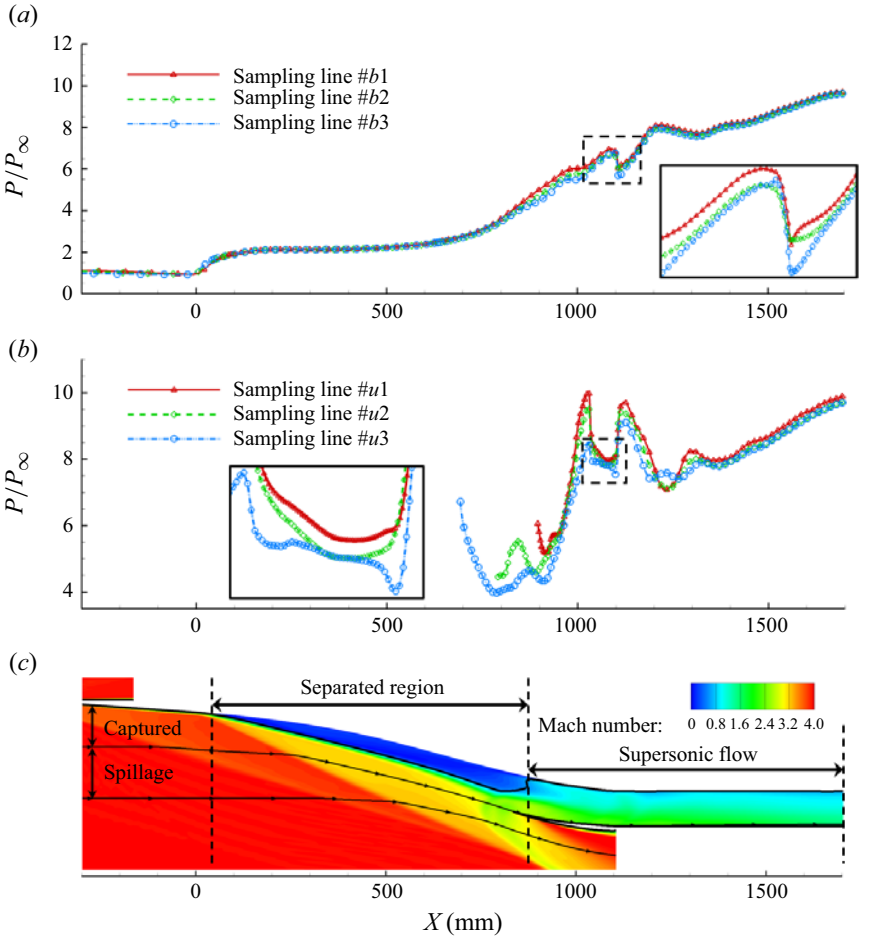

Figure 16. Time-averaged wall pressure distribution of sampling lines of the time-averaged flow field (*a*) on the upper and (*b*) bottom walls and (*c*) Mach number contours of the time-averaged flow field for slice $z = 0$. Pressure is normalized by the free-stream static pressure.

pressure drop and increase appear at $x = 1032.4$ mm and $x = 1105.1$ mm, which are caused by the shape trimming to ensure the smooth transition of the three-dimensional compression surface between the internal compression section and isolator. Furthermore, the bump causing a local pressure drop can reduce the pressure increase and thus inhibit the flow separation, which is beneficial for the overall performance of the REST inlet.

3.2. *Instantaneous flow organization*

From the results, the REST inlet unstart flow is highly unsteady and has significant characteristics of up–downstream coupling. The flow is affected by both the turbulence disturbance of the upstream boundary layer and backpressure caused by the downstream SWBLI simultaneously (Fu, Bose & Moin 2022). For a better understanding of the flow patterns, the Q criterion is selected for vortex visualization. The Q criterion is defined as

$$Q = \frac{1}{2}\left(\tilde{\Omega}_{ijij}\tilde{\Omega}_{ij} - \tilde{S}_{ij}\tilde{S}_{ij}\right), \tag{3.1}$$

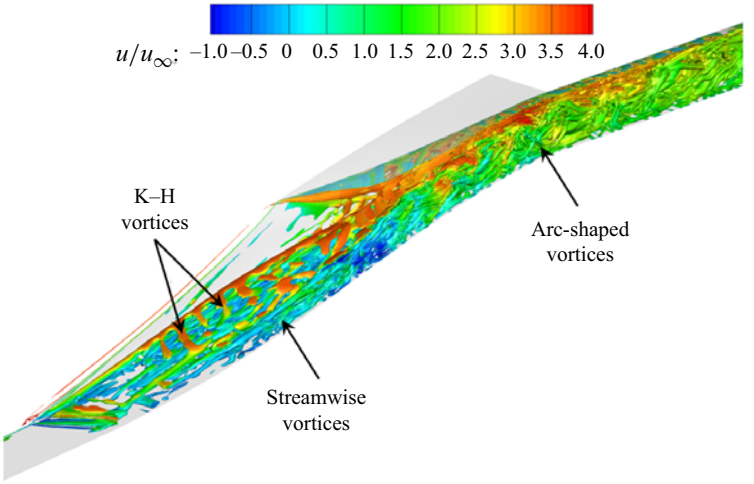

Figure 17. Instantaneous vortical structures at $tu_\infty/L = 8542.1$ visualized by iso-surfaces of $Q = 100$, coloured by the streamwise velocity.

where $\tilde{S}_{ij} = \frac{1}{2}(\partial\tilde{u}_i/\partial\tilde{x}_j + \partial\tilde{u}_j/\partial\tilde{x}_i)$ represents the symmetric part of the velocity gradient tensor while $\tilde{\Omega}_{ij} = \frac{1}{2}(\partial\tilde{u}_i/\partial\tilde{x}_j - \partial\tilde{u}_j/\partial\tilde{x}_i)$ is the antisymmetric part. In the region where $Q > 0$, the rotational rate of fluid is greater than the strain rate, and the flow is dominated by vortex structures.

Figure 17 displays the instantaneous flow organization of the computational domains visualized by the iso-surface of $Q = 100$ at $\langle t \rangle = tu_\infty/L = 8542.1$, time is normalized by the time that the fluid element takes to flow over the whole model with the free-stream velocity. From the results, there is no obvious vortex before the separation point. In contrast, vortical structures are generated over the bubble region. The typical Kelvin–Helmholtz (K–H) vortex structure can be observed near the shear layer and spanwise vortices are generated inside the separation bubble. After the separated region, the vortex structures perform as small-scale arc-shaped vortices affected by the shear layer instability and series of shock interactions. In addition, the arc-shaped vortices of the internal flow are not uniformly distributed but show a cyclical distribution trend along with the reflection of the shock wave in the isolator.

Except for the vortex structure, the separation shear layer is another important feature to scrutinize the dynamic motions of the instantaneous flow. Figures 18 and 19 display the streamwise velocity distribution for slice $z = 0$ and the velocity profile at different positions of the symmetry plane. When we take a closer look at the shear layer, there are negative and positive streamwise velocity fluctuations alternating along the shear layer, which is the most typical characteristic of the shear layer.

In order to illustrate the influence of the compressibility of the fluid on the shear layer, the convective Mach number is proposed and improved by Bogdanoff (1983) and Papamoschou & Roshko (1988). For a mixing layer where two gases on both sides have the same specific heat ratio, the convective Mach number M_c is defined as

$$M_c = \frac{u_1 - u_2}{a_1 + a_2}, \tag{3.2}$$

where u_1, u_2 and a_1, a_2 represent the flow velocities and local sound speeds for the two streams, respectively. For the supersonic flow, the flow structure of the shear layer is

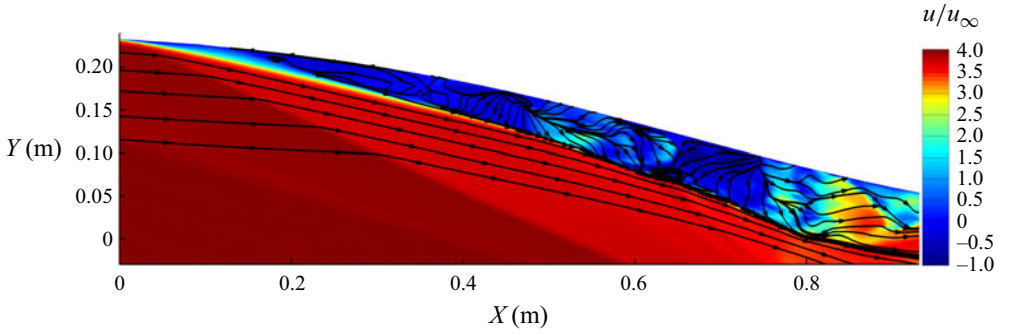

Figure 18. Contours of the instantaneous streamwise velocity for slice $z = 0$ at $tu_\infty/L = 8542.1$. The black arrow lines indicate the streamlines.

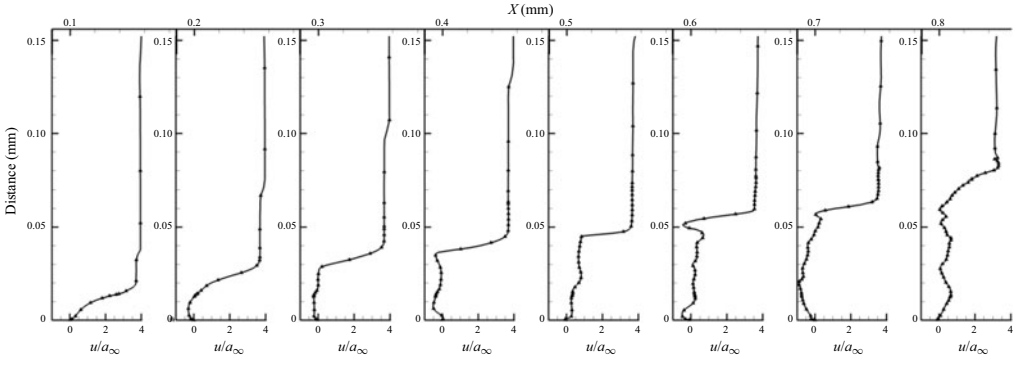

Figure 19. Streamwise velocity profile at probe points for slice $z = 0$ at $tu_\infty/L = 8542.1$. Streamwise velocity is normalized by the free-stream speed of sound.

associated with the convective motion of the large-scale structure with the free-stream flow (Papamoschou & Roshko 1988). Sandham & Reynolds (1990) proved that the flow structure shows clearly two-dimensional characteristics when $M_c < 0.6$, which is similar to the incompressible flow. In contrast, the shear layer has highly three-dimensional characteristics when $M_c > 0.6$ because of the three-dimensional instability and spanwise unstable waves. Figure 20 shows the vorticity thickness δ_w and convective Mach number M_c at probe points for slice $z = 0$ of the time-averaged flow and the instantaneous flow at $tu_\infty/L = 8542.1$. The vorticity thickness can be expressed by $\delta_w = \Delta U/|\mathrm{d}u/\mathrm{d}n|_{max}$, where ΔU is the difference in velocity of the shear layer and $|\mathrm{d}u/\mathrm{d}n|_{max}$ is the maximum velocity gradient. From the results, M_c is higher than 0.6 at all the probe points in the separated region. As indicated by Sandham & Reynolds, the compressible shear layer exhibits three-dimensional instabilities at this convective Mach number, which explains the emergence of oblique waves in the shear layer before the impinging point of the cowl-closure leading edge (CLE) shock and shear layer in figure 17. Also, because of the three-dimensional instability, an oblique wave as well as a spanwise flow structure is generated near $x = 500$ mm, causing δ_w and M_c to decrease, as shown in figure 20. In addition, after the formation of the K–H vortex, δ_w continuously increases while M_c decreases again at $x = 800$ mm. In the region near the impinging point, the interaction between the shear layer and the shock wave occurs, causing the shear layer instability accompanied by the large-scale vortices being broken into small-scale vortices. As a result,

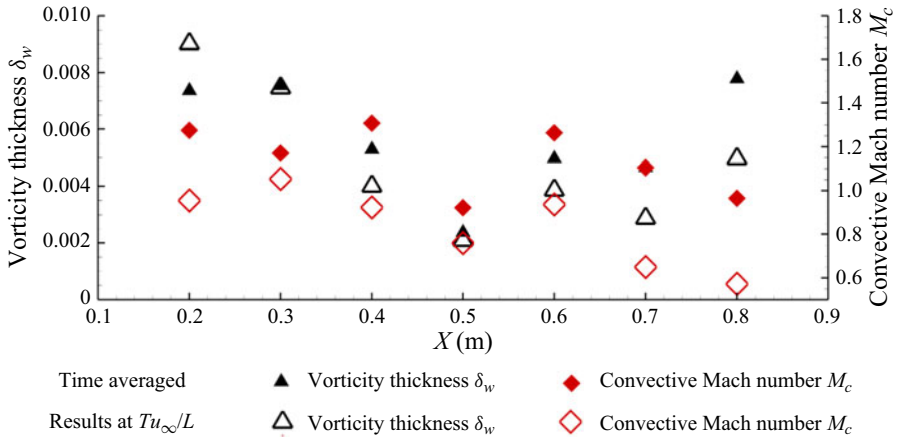

Figure 20. Vorticity thickness δ_w and convective Mach number M_c at probe points for slice $z = 0$ of time-averaged flow and instantaneous flow at $tu_\infty/L = 8542.1$.

the shear layer after the impinging point seems better mixed and the velocity gradient decreases, causing the increase of vorticity thickness, which is more significant in the instantaneous flow. Alternatively, due to the deceleration after the CLE shock, $u_1 - u_2$ decreases after the impinging point, leading to the decrease of convective Mach number at $x = 800$ mm in figure 20.

3.3. *Unsteady flow characteristics*

As described in the previous subsection, the unstart flow of the REST inlet is highly unsteady. To characterize the regions of most prominent unsteadiness, the variance of the velocity components is provided in figure 21. From the results, taking streamwise Reynolds stress $\langle u'u' \rangle$ for example, the most active region can be observed along the separated shear layer and after the impinging point, especially in the proximity of the impinging point with a maximum of approximately $1.74u_\infty$ at $x = 700.9$ mm, $y = 55.5$ mm, $z = 12.5$ mm. For the other normal Reynolds stress components $\langle v'v' \rangle$ and $\langle w'w' \rangle$, the high-level fluctuation is converged near the aft of the separation bubble, and the maximum of these two components is found further downstream than that of $\langle u'u' \rangle$. These major fluctuations are caused by the instability of the shear layer and separation bubble. The induced shock system and vortex structures enhanced the fluctuations of local flow, leading to the higher normal Reynolds stress. Additionally, relatively weak fluctuations are found along the separation shock, reflecting its unsteady position.

Except for these local flow phenomena, large-scale unsteady motion is identified in the unstart flow system. Figure 22 provides the instantaneous velocity field at two instants within a single cycle of the separation bubble motion, which also presents different states, i.e. expansion and shrinking of the bubble. Also, the position of the separation shock (marked as white iso-lines of $\partial P/\partial X$) moves, most notably in the shock foot region. At $tu_\infty/L = 3006.8$, the separation shock foot is located in the range $x = 101.7 \sim 140.8$ mm and the shock angle is $\eta = 22.9^\circ \sim 23.1^\circ$. At $tu_\infty/L = 3228.9$, the separation shock foot is located in the range $x = -0.5 \sim 17.8$ mm, and the shock angle decreases to $\eta = 21.1^\circ \sim 21.2^\circ$. It is clear from this comparison that the recirculation area and separation shock location vary in time. Moreover, the separation bubble thickness at $tu_\infty/L = 3228.9$ is smaller compared with that at $tu_\infty/L = 3006.8$. This is because of the increasing

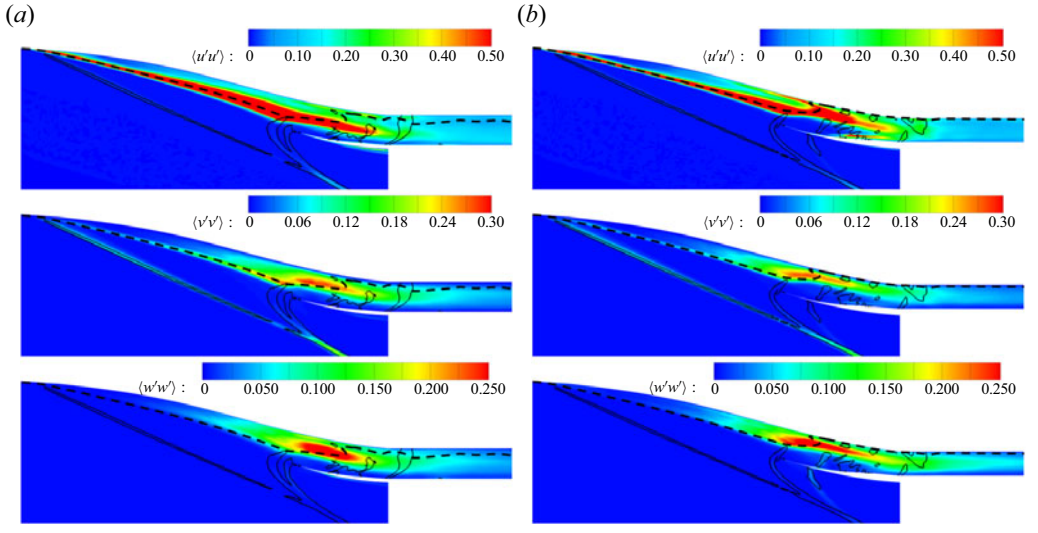

Figure 21. Contours of time-averaged variance of (*a*) plane at $z = 10$ mm and (*b*) plane at $z = 30$ mm. The black dashed and solid lines denote the isoline of $Ma = 1.0$ and $\partial P/\partial X = 25$.

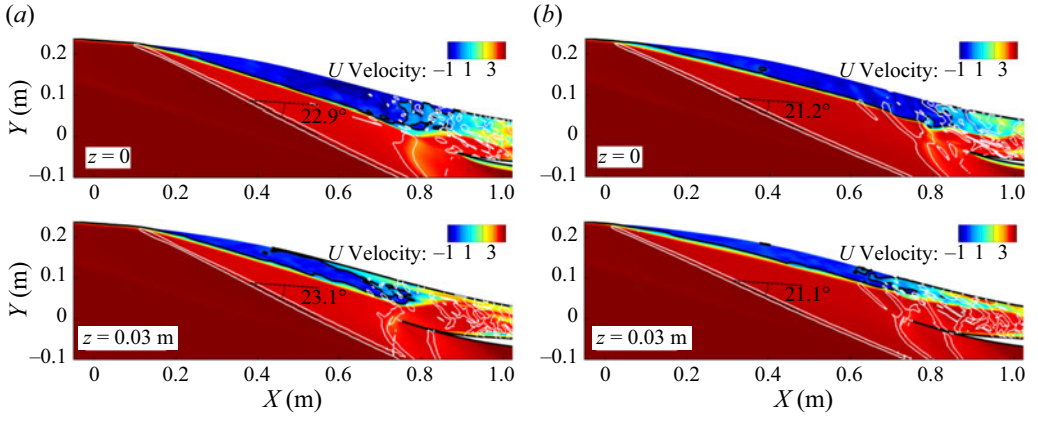

Figure 22. Contours of the instantaneous streamwise velocity for slice $z = 0$ mm and $z = 30$ mm at (*a*) $tu_\infty/L = 3006.8$ and (*b*) $tu_\infty/L = 3228.9$. The black solid line denotes the isoline of $u = 0$ and the white solid line signifies the isoline of $\partial P/\partial X = 25$.

interaction between the CLE shock and shear layer as the bubble moves upstream, which accelerates the instability of the shear layer and finally leads to the breaking of the bubble and reduction in the thickness (Zhong *et al.* 2023).

Figure 23 shows the contours of the instantaneous skin friction coefficient on the compression surfaces at $tu_\infty/L = 3006.8$ and $tu_\infty/L = 3228.9$, corresponding to the instants when the separation point is located at the forefront and rearward position within a single cycle motion, respectively. Also, the outline of the separation bubble is provided by the iso-line of $\langle C_f = 0\rangle$ in figure 23. From the results, distinctly different features can be observed in different regions of the unstart flow. In the upstream region of the flow separation, $\langle C_f = 0\rangle$ is homogeneously distributed. By contrast, clear evidence of the spanwise preferential orientation of the near-wall coherent structures can be observed within the separation bubble. Downstream of the reattachment, streamwise-oriented

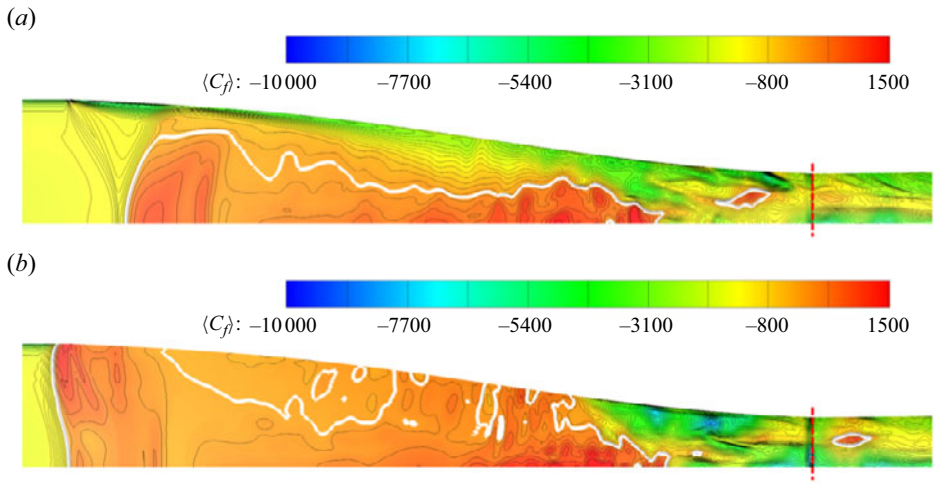

Figure 23. Contours of instantaneous skin friction on the compression surfaces at (*a*) $tu_\infty/L = 3006.8$ and (*b*) $tu_\infty/L = 3228.9$. The solid red line indicates the throat location and the dashed white line indicates the boundary of the separation region ($\langle C_f \rangle$).

features can be found, which indicate large-scale streaks with a spanwise alternation of high and low velocity.

The spanwise alternatively distributed low and high skin friction streaks after the reattachment are believed to be induced by the up-wash and down-wash effects of the streamwise vortices. Figure 24(*a*) provides the contours of skin friction on the compression surfaces and X-vorticity of specific slices at $tu_\infty/L = 3228.9$. It should be clarified that the slices in figure 24(*a*) are converted into rectangular format for a better understanding of the up- and down-wash effects of the streamwise vortices. As shown in figure 24(*a*) and described in the previous subsection, the near-wall flow after the reattachment is dominated by the streamwise structures with the breaking of the separation bubble. As a result, the wall skin friction between two adjacent streamwise vortices would be enhanced or weakened affected by the down-wash or up-wash effects, as illustrated in figure 24(*b*). Also, figure 24(*c*) provides the power spectral density (PSD) of averaged $\langle C_f = 0 \rangle$ at three stations at $x = 135$ mm, $x = 900$ mm and $x = 950$ mm. Downstream of the separation point, i.e. $x = 135$ mm, broadband low-frequency content can be observed, corresponding to the unsteady breathing of the separation bubble. However, the amplitude of this low frequency is very small at the aft of the bubble. Along the streamwise distance, two significant medium frequencies can be identified, of which the higher one is around $St = fd/u_\infty = 0.00116$ and the lower one is around $St = fd/u_\infty = 0.00084$. The amplitude of these two characteristic medium frequencies increases gradually along the streamwise distance, especially downstream of the attachment.

Moreover, streamwise alternatively distributed low and high skin friction streaks can be found before the reattachment from figure 23, although this pattern is indistinct. It seems to suggest that the flow structures dominating the local flow field are the spanwise flow structures upstream of the reattachment, whereas streamwise flow structures are dominating the local flow field downstream of the reattachment. The dominant spanwise wavelength is $\lambda_z \approx 0.5h_t$ (h_t donates the diameter of the throat), which is very close to the dominant streamwise wavelength. From the results, the transition of the characteristic flow structure seems to be an important issue for the REST inlet to maintain a self-sustaining unstart flow. Detailed mechanisms for it will be investigated in the following subsection.

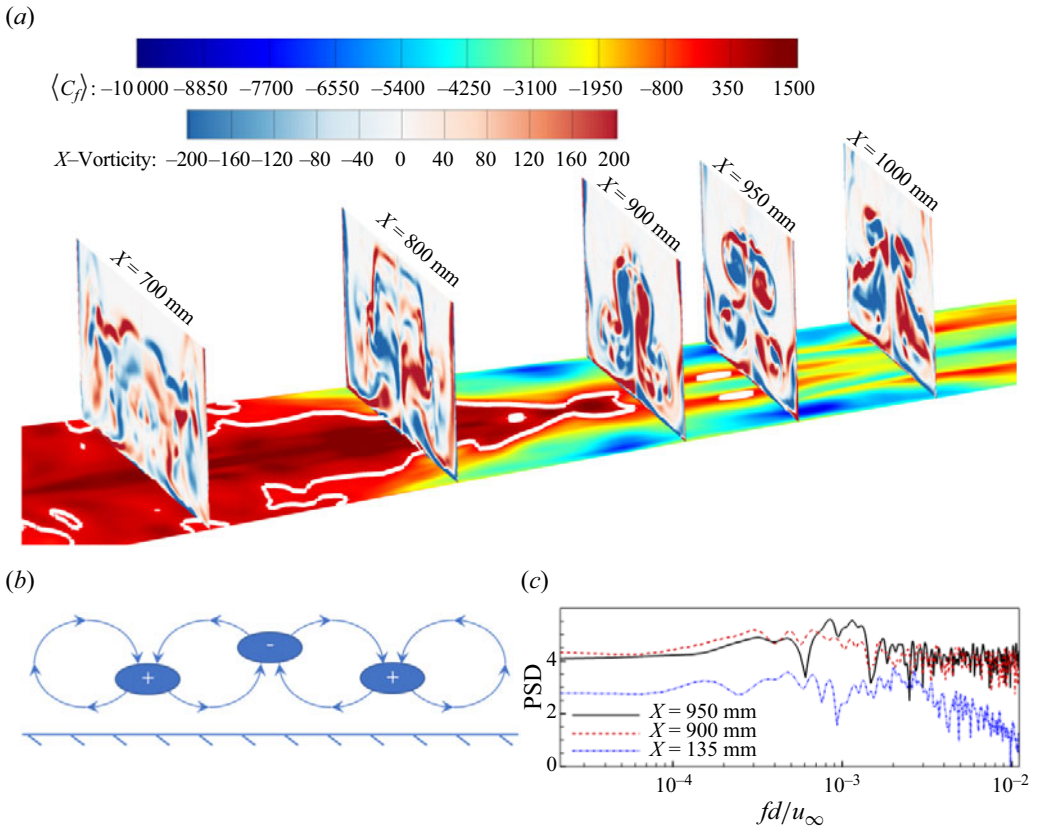

Figure 24. (*a*) Contours of instantaneous skin friction on the compression surfaces and X-vorticity of specific slices at $tu_\infty/L = 3228.9$. The solid white line indicates the boundary of the separation region. (*b*) Schematic diagram for the up- and down-wash effects of the alternating distributed streamwise vortices. The positive and negative symbols indicate that the region is affected by down-wash and up-wash effects, respectively. (*c*) Power spectral density of averaged $\langle C_f \rangle$ at $x = 135$ mm, $x = 900$ mm and $x = 950$ mm.

3.4. *Spectral analysis*

For the further analysis of the unsteady characteristics of the REST inlet under the off-design operating condition, an overview of frequency characteristics for the separated region and the downstream flow structures is provided by the PSD of the wall pressure at selected probe points on the sampling lines in figure 25. Notably, the unsteady characteristics are quantified by the non-dimensional Strouhal number $St = fd/u_\infty$ based on the inlet length and free-stream velocity. The locations of the probe points and the sampling lines have already been introduced in § 3.1. The further downstream in the station, the more high-frequency signals there are and the difference between the upper and the lower walls is gradually decreasing. In the aft of the isolator, the PSDs of the upper and the lower wall are even identical, which is consistent with our previous study (Zhong *et al.* 2023). The instability of the shear layer and the separation bubble accelerates the averaging process of the downstream flow, leading to the high level similar PSDs at the aft of the isolator.

When we take a closer look at the upstream stations, the high-frequency characteristics are not obvious, indicating that the flow is dominated by large-scale flow structures

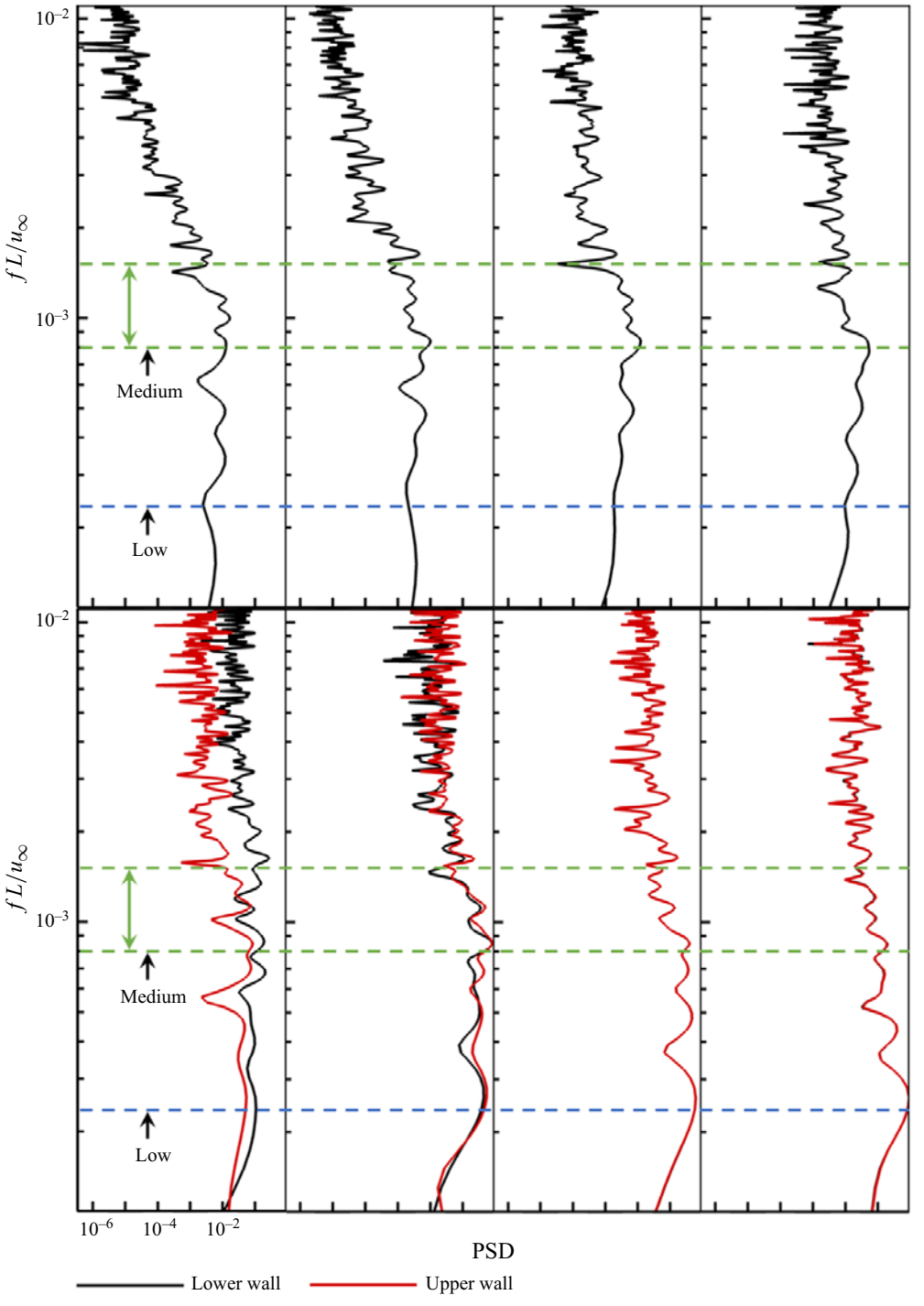

Figure 25. The PSDs of the wall pressure with the streamwise distance on the upper and lower walls.

including the breathing of the separation bubble and the unsteady movement of the separation shock wave. With the flow developing downstream, a significant increase in the medium-frequency fraction can be observed, where instability of the separated shear layer

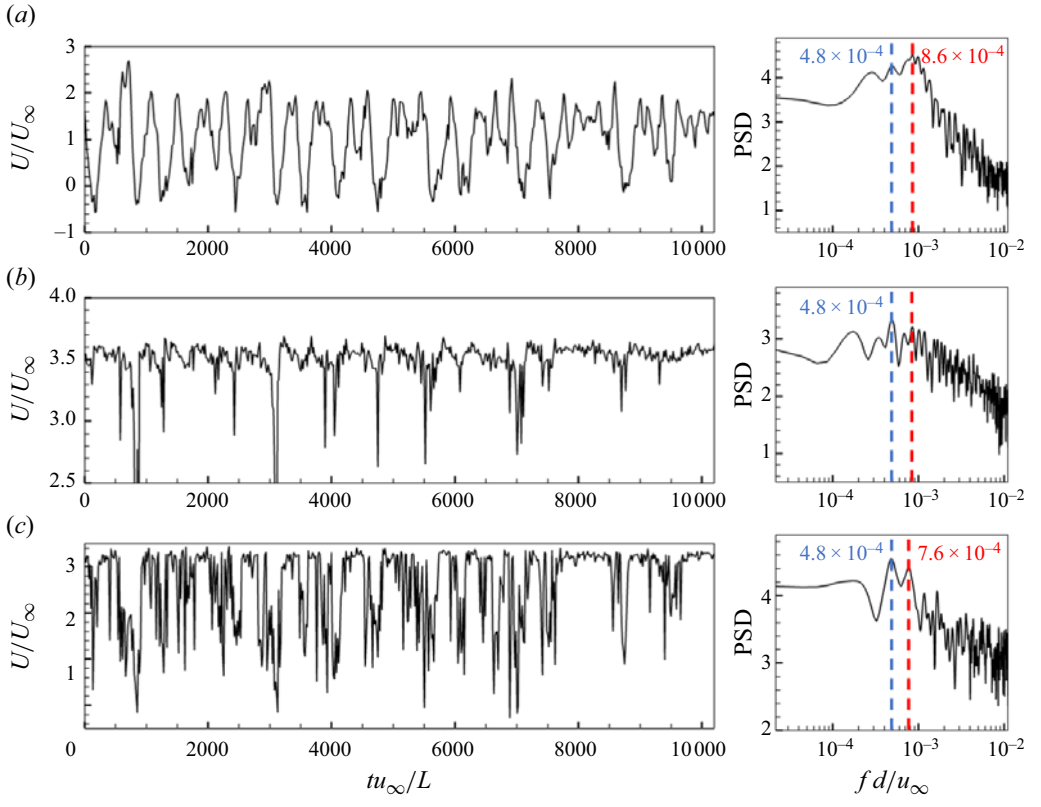

Figure 26. Temporal evolution and corresponding PSDs of streamwise velocity within the shear layer at (*a*) $x = 300$ mm, $y = -64$ mm, (*b*) $x = 700$ mm, $y = -201$ mm, (*c*) $x = 900$ mm, $y = -229$ mm.

occurs and the shedding vortices are formed. In a SWBLI system, these medium-frequency motions are proved to be associated with relatively small-scale flow structures, such as the shedding of the shear layer vortices, compared with the low-frequency motions (Hu *et al.* 2021). In the current study, the enhanced medium-frequency motions are caused by the instability of the separated shear layer and the induced shedding vortices. After the impinging point of the CLE shock and the shear layer, the shear layer and the separation bubble rapidly becomes unstable and the shedding vortices break into small-scale vortices. As a result, the flow further downstream is dominated by high-frequency motions.

Except for the wall pressure signals, the temporal evolution and corresponding PSD of streamwise velocity within the shear layer at several prove points are shown in figure 26. At the upstream stations, the regularity of streamwise velocity is more obvious. In contrast, a sharp decrease and sharp increase of the streamwise velocity can be observed at downstream stations, and the decrease process takes more time while the increase occurs in a very short time. This phenomenon is corresponding to the formation of the shedding vortices. The instability of the shear layer and the vortex shedding cause the increase and decrease of the separation bubble thickness, causing the decrease and increase of the streamwise velocity, respectively.

In terms of spectral characteristics, the upstream flow is dominated by low-frequency motions. A low-frequency peak in PSD can be observed at $St = 4.8 \times 10^{-4}$, which is basically fixed at each station. Alternatively, another higher-frequency peak can be

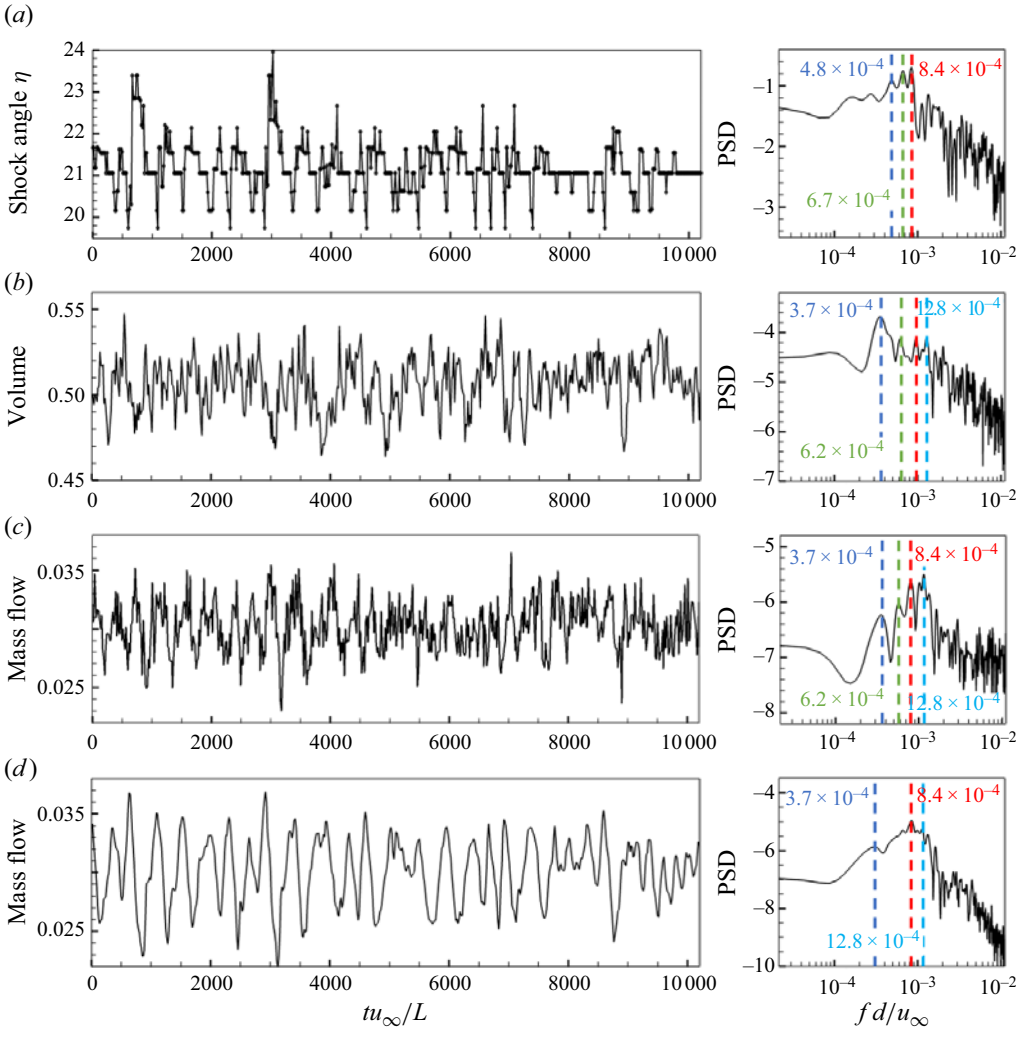

Figure 27. Temporal evolution and corresponding PSD of (*a*) separation shock angle η, (*b*) volume of separation bubble, (*c*) mass flow through isolator, (*d*) total captured mass flow.

observed at $St = 7.6 \sim 8.6 \times 10^{-4}$ and it increases at the downstream locations affected by the instability of the shear layer.

With regard to the global dynamics, the temporal variation of the separation shock angle and the volume of the separation bubble are shown in figure 27. Notably, the shock angle is obtained according to the slope of a segment. The two endpoints of this segment are the mid-point of the intersections between two fixed sampling lines and the isoline of $\partial P/\partial X$. As a result, the value of the shock angle is a series of discrete points, causing the values to converge around several certain values, as shown in figure 27(*a*). However, this approach will affect more the high-frequency characteristics of the data but have less impact on the low-frequency characteristics, which is what we are concentrating on. The same approach is also adopted in Hu *et al.* (2021) when obtaining the shock angle. Therefore, this approach to obtaining the shock angle is considered to be feasible. Another value, the volume of the separation bubble, is defined as the volume of the region within the

iso-surface of $u = 0$ and the wall. From the results, two frequency peaks, $St = 4.8 \times 10^{-4}$ and $St = 8.4 \times 10^{-4}$, can be identified from the PSD of the separation shock angle. These two characteristic frequencies are the same as those in the previous analysis. Except for these two frequency peaks, a third medium frequency peak $St = 6.7 \times 10^{-4}$ can be observed. In the same way, three frequency peaks, $St = 3.7 \times 10^{-4}$, $St = 6.2 \times 10^{-4}$ and $St = 12.8 \times 10^{-4}$ can be identified from the PSD results of the separation bubble volume. For both the shock angle and the volume of the separation bubble, some extra characteristic frequencies, $St = 6.2 \times 10^{-4}$, $St = 6.7 \times 10^{-4}$ and $St = 12.8 \times 10^{-4}$, can be observed compared with the results shown in figure 26, which seem to be dominated by the instability of the shear layer and the shedding vortices. As explained previously, the subsonic region in the whole computational domain consists of the separation region and the shedding vortices. Moreover, the formation of shedding vortices is usually accompanied by variations in the separation thickness and the separation shock angle. Therefore, these medium-frequency peaks can be considered to be dominated by the instability of the shear layer and shedding vortices. Furthermore, this explained why the second frequency peak in figure 26 increases at downstream stations.

Furthermore, the temporal variations of the mass flow through the isolator and the captured mass flow of the inlet are also provided in figure 27. Among them, the captured mass flow can be categorized into two components, one of which is used to sustain the scale of the separation bubble and another goes directly through the isolator. From the results, both the mass flow and the captured mass flow share identical periodicity and mean value, while the captured flow exhibits more periodic and regular fluctuations. This is because the captured mass flow is influenced only by the separation point location and the separation shock angle. Consequently, two frequency peaks, $St = 6.7 \times 10^{-4}$ and $St = 8.4 \times 10^{-4}$, can be observed in figures 27(*c*) and 27(*d*), which are the same as those of the shock angle. In addition to this, $St = 3.7 \times 10^{-4}$, $St = 5.8 \times 10^{-4}$ and two frequency peaks around $St = 12.8 \times 10^{-4}$ can be identified, which are close to the dominant frequency of the separation bubble volume. This finding demonstrates that the mass flow is influenced not only by the movement of the separation point and the flapping motion of the separation shock, but also by the vortex shedding. Furthermore, it explained why the mass flow exhibits higher-frequency characteristics compared with the captured flow, as depicted in figure 27(*d*). It can be also evidenced by the following coherence analysis of figure 29, where the mass flow and the separation bubble volume demonstrate high coherence in the above frequencies. Upon comparing the mass flow and the total captured mass flow, it is observed that up to 24.18 % of the captured flow is prevented from entering the isolator because of the maintenance of the separation bubble. For this, the effects of the separation bubble and shear layer instabilities on the flow capture characteristic of the inlet in an unstart flow cannot be disregarded in practical applications.

To confirm the connection between the low- and medium-frequency motions and the flow patterns, several flow parameters are extracted from the current result and statistical analysis is carried out via the coherence C_{xy} and phase θ_{xy}

$$C_{xy}(f) = \left|P_{xy}(f)\right|^2 / \left(P_{xx}(f)P_{yy}(f)\right), \quad 0 \leqslant C_{xy} \leqslant 1, \tag{3.3}$$

$$\theta_{xy}(f) = \mathrm{Im}\left\{P_{xy}(f)\right\} / \mathrm{Re}\left\{P_{xy}(f)\right\}, \quad -\pi \leqslant \theta_{xy} \leqslant \pi. \tag{3.4}$$

In which P_{xx} is the PSD of $x(t)$, and P_{xy} indicates the cross-PSD between $x(t)$ and $y(t)$. For a certain frequency, the relation between two signals is not linear or there is noise in the datasets if $0 < C_{xy} < 1$. When $C_{xy} = 1$, $x(t)$ and $y(t)$ are linearly related. Conversely, $C_{xy} = 0$ signifies that these two signals are completely unrelated.

The coherences and phases between the separation shock angle and several parameters extracted from the computational domains are provided in figure 28. The definitions of the separation shock angle and the volume of the separation bubble are the same as before. In figure 28(*a*), two high values of coherence ($C_{xy} = 0.82$ and $C_{xy} = 0.83$) are observed at the frequencies $St = 7.3 \times 10^{-4}$ and $St = 15.9 \times 10^{-4}$ with large phases of $\theta = 0.679\pi$ and $\theta = 0.798\pi$, which signifies that the shock angle and the separation point are highly related to each other around the dominant low and medium frequencies in figure 27. This is predictable since the shock angle and the separation point are both related to the scale and location of the separation bubble. With the separation bubble moving downstream, the thickness of the separation bubble increases, accompanied by the increases in the shock angle. Also, figures 28(*b*) and 28(*c*) indicate that the streamwise velocity within the shear layer and the volume of the bubble are nonlinearly related to the shock angle around the dominant low and medium frequencies. In the same way, the formation of shedding vortices can be reflected by the volume of the separation bubble and the velocity within the shear layer at downstream stations, which has been proven in the previous analysis. Another study of our previous work about the unsteady mechanism for inlet unstart flow at the off-design condition also indicates that the influence of the shedding vortices can propagate upstream within the subsonic region and influence the scale and location of the separation bubble, which will further affect the separation point and shock angle (Zhong *et al.* 2023). The above observations demonstrate that the unsteady low-frequency behaviour is related to the breathing of the separation bubble and the flapping motion of the separation shock wave, while the medium-frequency motions are associated with the shedding vortices of the shear layer. For this, a decoupling of the frequency scales is required to further trace the sustained source of the intrinsic unsteadiness of inlet unstart flow, which is the objective of the next subsection.

3.5. *Dynamic mode decomposition analysis of the three-dimensional flow field*

To better investigate the low-frequency dynamics of the REST inlet unstart flow from the coupled broadband-frequency spectrum, a modal decomposition of the three-dimensional flow field is performed based on DMD. Figure 30(*a*) displays the eigenvalue spectrum of DMD. From figure 30(*a*), all the eigenvalues for both pressure fluctuation and X-velocity fluctuation results are distributed near the unit circle, indicating that all the modes decoupled from the unstart flow are quasi-stable modes. This is predictable from the temporal results in §§ 3.3 and 3.4 since each parameter is quasi-periodically distributed in a fully evolved unstart flow.

From the frequency-magnitude spectrum, a main mode and three characteristic modes are selected from the frequency spectrum based on the analysis above, as shown in table 5. The dominant frequency of the main mode ϕ_1 is basically coincident with the dominant frequency of the unstart flow of Trapier's studies (Trapier, Deck & Duveau 2008). Figure 31 displays the real part of the main mode ϕ_1 with iso-surfaces of the pressure fluctuation at two different phase angles. At these two instants, the prime feature of the modal fluctuation is the structure along the compression waves, including the separation shock, CLE shock and the shock series within the internal flow. Comparing the modal fluctuations at these phase angles, the separation shock continuously exists while the shock series within the internal flow exists intermittently since the internal flow is influenced by the flow structures around the reattachment. As a result, the shock strings make a large contribution to the overall flow only at certain phases. Figure 32(*a*) gives

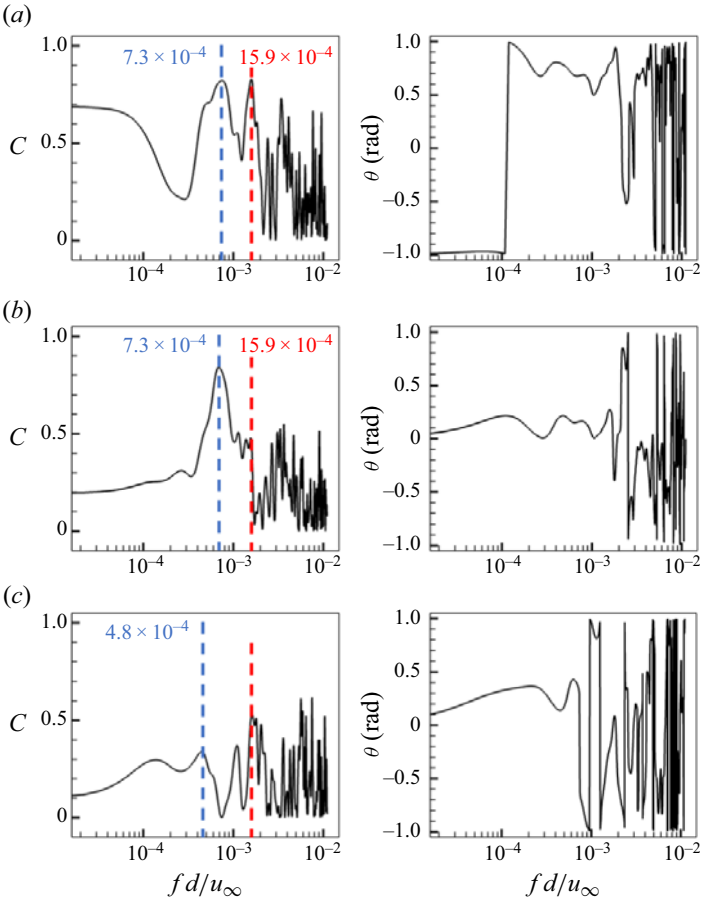

Figure 28. Coherence and phase between separation shock angle η and (*a*) separation point, (*b*) streamwise velocity at $x = 300$ mm, $y = -64$ mm, (*c*) volume of the separation bubble.

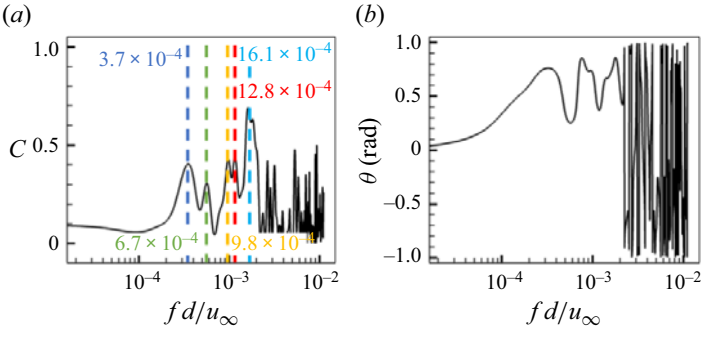

Figure 29. Coherence and phase between the volume of the separation bubble and mass flow through the isolator.

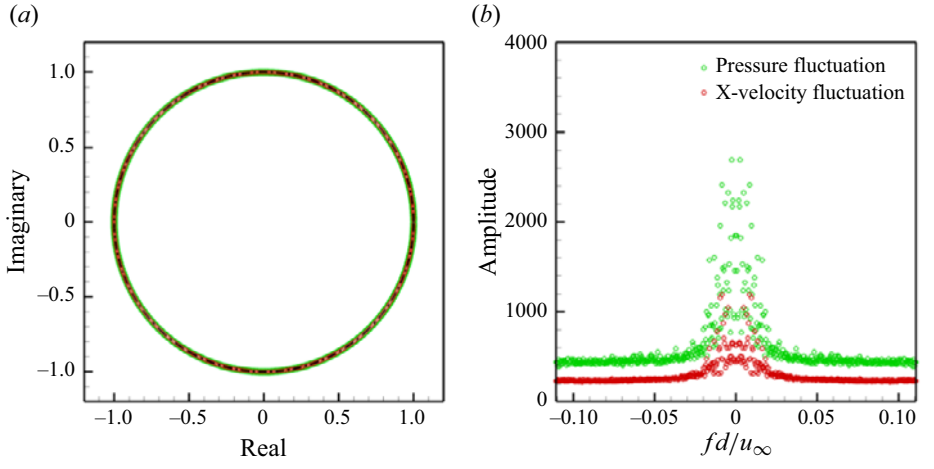

Figure 30. (*a*) Eigenvalue spectrum from DMD and (*b*) mode amplitudes at different frequencies.

Mode	S_t	Pressure Amplitude	U-Velocity Amplitude
ϕ_1	8.51×10^{-3}	2415.2	1190.5
ϕ_2	3.70×10^{-4}	1853.2	626.33
ϕ_3	7.50×10^{-4}	1457.9	480.87
ϕ_4	1.11×10^{-3}	933.74	465.17

Table 5. Information of the selected modes.

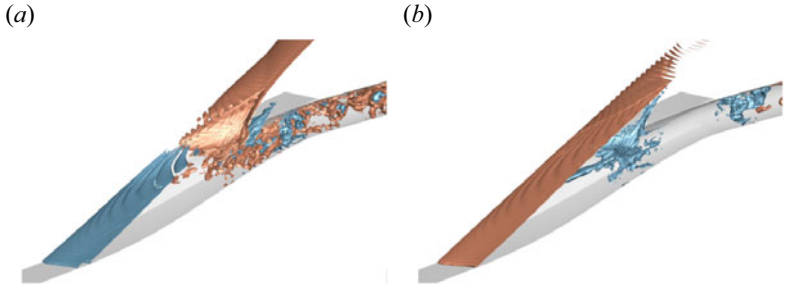

Figure 31. Isosurfaces of the pressure fluctuations from DMD mode ϕ_1 with phase angle (*a*) $\theta = \pi/2$ and (*b*) $\theta = 3\pi/4$, only including the real part (red: $p'/p = 0.0003$, blue: $p'/p = -0.0003$).

the modal of pressure fluctuation on the slice $z = 0$ in which the effect of shocks and compression waves in mode ϕ_1 is more clear.

Figure 33 gives the modal fluctuation of the streamwise velocity of the main mode ϕ_1 at two different phase angles similar to figure 31. Compared with the modal fluctuation of pressure, the key features are centralized around the shear layer and the downstream flow, where active vortices occur. Large fluctuations are streamwise distributed and are mainly distributed around the shear layer and near-wall region, as shown in figure 32(*b*). Other modes with similar frequency to ϕ_1 are also examined, the large fluctuations can be observed around the compression waves from DMD of the pressure fluctuation. In the

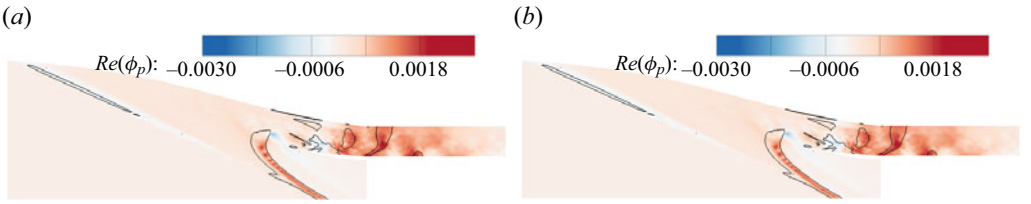

Figure 32. Real part of DMD mode ϕ_1 indicating contours of modal (*a*) pressure fluctuations and (*b*) streamwise velocity fluctuations on the slice $z = 0$. The black solid line indicates the location of shock wave visualized by isoline of $\partial P/\partial X$ from the mean flow.

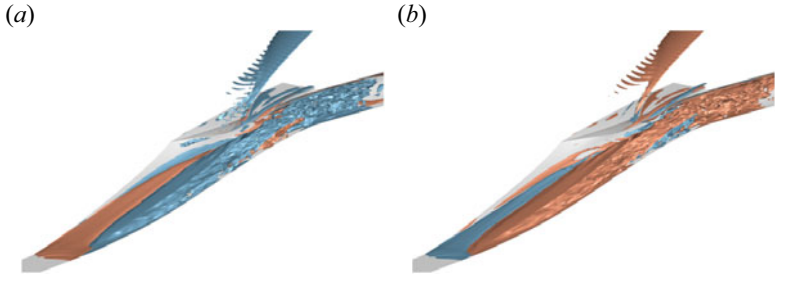

Figure 33. Isosurfaces of the streamwise velocity fluctuations from DMD mode ϕ_1 with phase angle (*a*) $\theta = \pi/2$ and (*b*) $\theta = 3\pi/4$, only including the real part (red: $p'/p = 0.0003$, blue: $p'/p = -0.0003$).

same way, the motion of the shear layer can be observed in the results of streamwise velocity fluctuation, indicating that the separation bubble and separation shock are the most significant flow patterns for the REST inlet unstart flow, as can be seen in figure 21. In addition, an obvious structure can be observed outside the cowl lip, which is caused by the streamwise vertices induced by the spillage around the cowl-closure leading edge. In an experimental study of the inward-turning inlet by Li *et al.*, the same flow structure is also observed by schlieren and this flow structure is proved to have a significant influence on the downstream flow (Yiming *et al.* 2021). However, the spillage and streamwise vertices within the outflow are out of the scope of the current study. Detailed information about it can be found in Yiming *et al.* (2021), Zhang, Li & Yang (2021) and Wang *et al.* (2018).

For mode ϕ_2, the pressure fluctuations visualized by the isosurfaces are shown in figure 34, in which the fluctuations with high levels are mainly distributed along the CLE shock and shock series around the reattachment. Compared with mode ϕ_1, the periodicity of the fluctuation is more obvious downstream of the reattachment, indicating that the three-dimensional feature in ϕ_2 is also stronger than that in ϕ_1. Large and small fluctuations are alternately distributed in the streamwise direction, revealing a propagation of waves from the impinging point of the shear layer and CLE shock and outwards along the shock waves. From the pressure fluctuations distribution of symmetry in figure 35(*a*), the radiation of waves along the streamwise and shock can be observed more obviously.

In comparison, the streamwise velocity fluctuations are displayed in figure 36. Smaller-scale vortical structures can be observed compared with ϕ_1. These vortical structures are mainly distributed along the streamwise direction and show small periodicity in the spanwise direction. This is because the evolution of the streamwise vortices is limited by the side-wall and compression surfaces, causing the small periodicity in the spanwise direction. Furthermore, the distribution of the streamwise velocity fluctuations shows high similarity to the skin friction distribution on the compression surfaces in

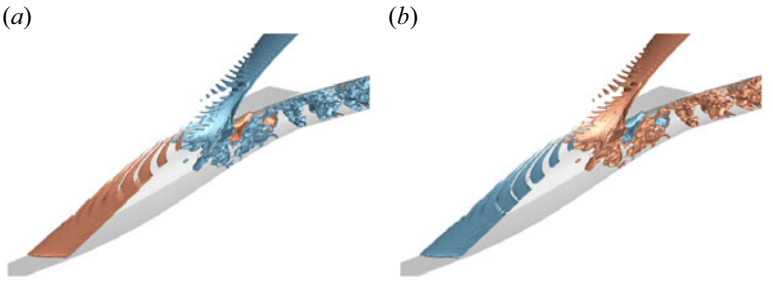

Figure 34. Isosurfaces of the pressure fluctuations from DMD mode ϕ_2 with phase angle (*a*) $\theta = \pi/2$ and (*b*) $\theta = \pi$, only including the real part (red: $p'/p = 0.0003$, blue: $p'/p = -0.0003$).

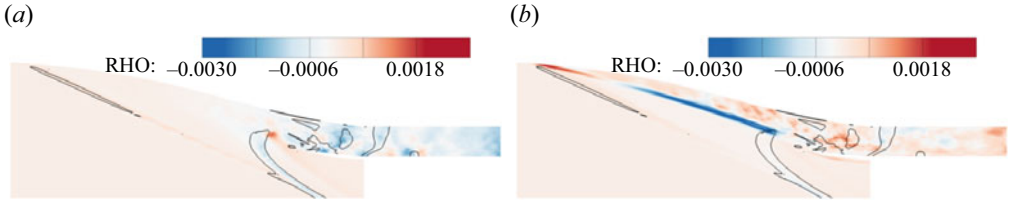

Figure 35. Real part of DMD mode ϕ_2 indicating contours of modal (*a*) pressure fluctuations and (*b*) streamwise velocity fluctuations on the slice $z = 0$. The black solid line indicates the location of shock wave visualized by isoline of $\partial P/\partial X$ from the mean flow.

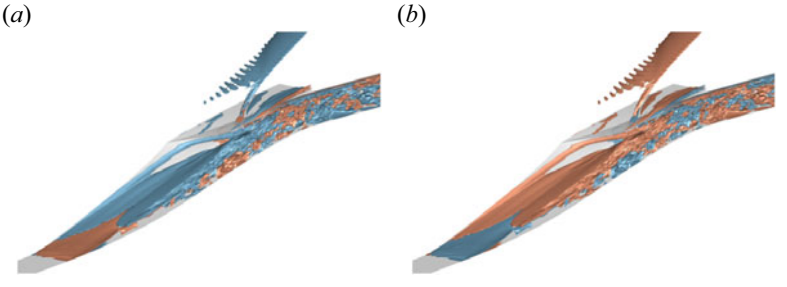

Figure 36. Isosurfaces of the streamwise velocity fluctuations from DMD mode ϕ_2 with phase angle (*a*) $\theta = \pi/2$ and (*b*) $\theta = \pi$, only including the real part (red: $p'/p = 0.0003$, blue: $p'/p = -0.0003$).

figure 24. From the motion of reconstructed flow based on ϕ_2, the propagation of the disturbance starting from the reattachment of the bubble and the shedding vortices is obvious, indicating that this mode, as well as the low-frequency motion, are associated with the breathing of shock waves and motion of the shear layer.

For the mode ϕ_3 with higher dominant frequency, which is associated with the motion of shedding vortices, the pressure fluctuations and streamwise velocity fluctuations are shown in figures 37 and 38. From the results, the pressure fluctuations are centred around the CLE shock wave and the reattachment, indicating that mode ϕ_3 with higher frequency is related to the motion of shedding vortices. At the same time, the streamwise velocity fluctuations are elongated and distributed in the streamwise direction, which reveals that the motion of shedding vortices is associated with the generation of streamwise structures around the reattachment. Furthermore, the results illustrate that the effect of the CLE shock on the shear layer is to accelerate the instability of the shear layer and thus the shedding

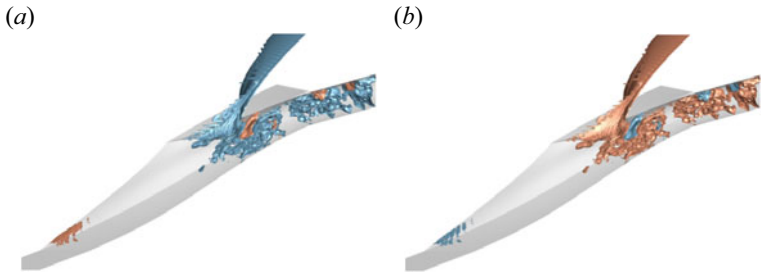

Figure 37. Isosurfaces of the streamwise velocity fluctuations from DMD mode ϕ_3 with phase angle (*a*) $\theta = \pi/2$ and (*b*) $\theta = \pi$, only including the real part (red: $p'/p = 0.0003$, blue: $p'/p = -0.0003$).

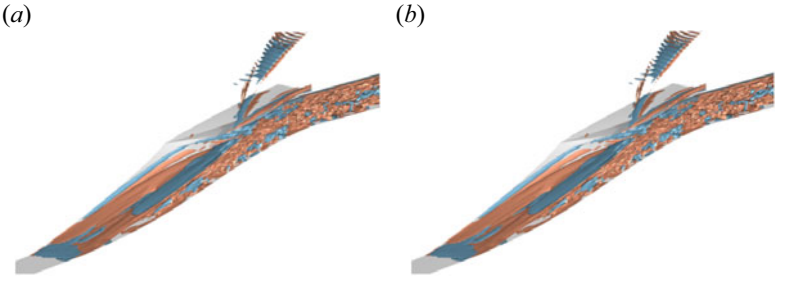

Figure 38. Isosurfaces of the streamwise velocity fluctuations from DMD mode ϕ_4 with phase angle (*a*) $\theta = \pi/2$ and (*b*) $\theta = \pi$, only including the real part (red: $p'/p = 0.0003$, blue: $p'/p = -0.0003$).

vortices are formed. In other words, the CLE shock plays an important role during the dominant flow structure converting from spanwise backflow within the separated region to streamwise vortices around the reattachment, as shown in figures 23 and 24.

4. Physical mechanism of REST inlet unstart flow

In comparison with the traditional two-dimensional or quasi-two-dimensional SWBLI configurations, the flow topology of the REST inlet unstart flow shows significantly different features. In the canonical impinging shock, ramp shock, forward- and backward-facing step cases, the geometry and flow topology are relatively simpler and the separation bubble is induced by only a single oblique shock or the step. Alternatively, the REST inlet consists of irregular compression surfaces generated by a comprehensive consideration of streamline tracking and shape transition rather than the multiple ramps in the two-dimensional case, leading to significant differences in the flow structure in the unstart flow. In REST inlet unstart flow, a large-scale separation bubble is located on the compression surfaces with a separation shock in front of the bubble. Near the maximum thickness of the bubble, a CLE shock induced by the CLE interacts with the shear layer and accelerate the instability of the shear layer. Downstream of the separated region, the flow performs as small-scale arc-shaped vortices affected by the shear layer instability and series of shock interactions.

The instantaneous flow visualized in 3.3 illustrates the localized and global unsteady motion of the REST inlet unstart flow under the off-design condition, which involves the oscillation of separation shock, breathing of the separation bubble, the interaction between the CLE shock and shear layer, instability of the shear layer and the formation of the shedding vortices. Also, the result indicates that the most unstable global mode is

mainly distributed around the shear layer and the region where the shedding vortex occurs. The spectral analysis in 3.4 reveals that there are two types of low frequencies around $St = 4 \times 10^{-4}$ and $St = 7 \times 10^{-4}$, corresponding to the coupling of the breathing bubble and the oscillation of the separation shock. A higher medium frequency is associated with the shedding vortices. These can be also visualized by the streamwise velocity and pressure fluctuation from three-dimensional DMD analysis and the contribution of each selected characteristic mode reveals the contribution of a specific flow structure to the low- and medium-frequency interaction. Apart from the unsteady separation bubble and shedding vortices, the DMD mode also reveals the transition from spanwise-dominated flow to streamwise-dominated flow motion downstream of the separation. In both instantaneous flow and DMD mode, 'Görtler-like vortices' are observed. However, the formation and evolution of the Görtler vortices are limited due to the large contraction ratio in the spanwise direction of the REST inlet, thus only a counter-rotating vortex pair (CVP) and seldom small-scale streamwise vortices are formed, as shown in figures 36 and 37. However, the CVP produces a similar effect on the unstart flow. During the whole process when the flow undergoes the localized and global unsteady motions, the separation bubble is required to remain within a certain scale and location. In other words, the shear layer instability and shedding vortices will strip mass from the separation bubble. Therefore, another way in the flow field exists to replenish the mass of the separation bubble opposite to the shedding vortices. From the flow structure and unsteady motion on the unstart flow, it seems that the flow is injected into the separation bubble and becomes part of the backflow inside the bubble affected by the flow structures around the reattachment. Thus, the scale and location of the separation bubble maintain dynamic equilibrium.

We believe that the low- and medium-frequency mode transition is associated with the self-sustaining of the separation bubble. Around the reattachment, the main flow structure converts from spanwise backflow into streamwise vortices, as shown in figures 23 and 24. Affected by the up- and down-wash effects of the CVP, low and high skin friction streaks are formed downstream of the reattachment. Further, the streamwise vortices accelerate the process of downstream flow averaging, causing similar spectral characteristics at downstream stations in figure 25. For the CVP, the mechanism of their generation is displayed in figure 39. As shown in figures 39(*b*) and 39(*c*), the shedding vortices are formed and developed centred on symmetry. As a result, the backflow of the shedding vortex produces an up-wash effect on the flow near the wall around the reattachment. Affected by the up-wash effect and spanwise instability of the shear layer, the CVP is formed.

Estruch-Samper and Chandola proposed an entrainment–recharge mechanism to associate low-frequency unsteadiness with the shedding effects (Estruch-Samper & Chandola 2018). In this theory, the bubble's decay–growth dynamics is associated with the low-frequency mechanism by the shear layer's motion and the Strouhal number of the low-frequency breathing can be related to the entrainment frequency as

$$St_r^{low} = \pi \alpha_\varepsilon \xi_B \delta'^2 \frac{L_r}{h} \left(X_r^{ent}\right)^2 St_r^{ent} \approx C_\varepsilon \frac{L_r}{h} \left(X_r^{ent}\right)^2 St_r^{ent}, \tag{4.1}$$

where α_ε is the length-to-thickness ratio of the shedding coherent structures, ξ_B signifies the percentage of the entrainment mass and δ' is the spreading rate of the mixing layer. Huang *et al*. have proved that the difference between these three variables in different cases is small, thus the multiplication of these three parameters can be considered as a constant $C_\varepsilon = \alpha_\varepsilon \xi_B \delta'^2$. Also, L_r/h is the ratio of the bubble length to bubble height and X_r^{ent} is the non-dimensional entrainment length which depends on the specific geometry and flow

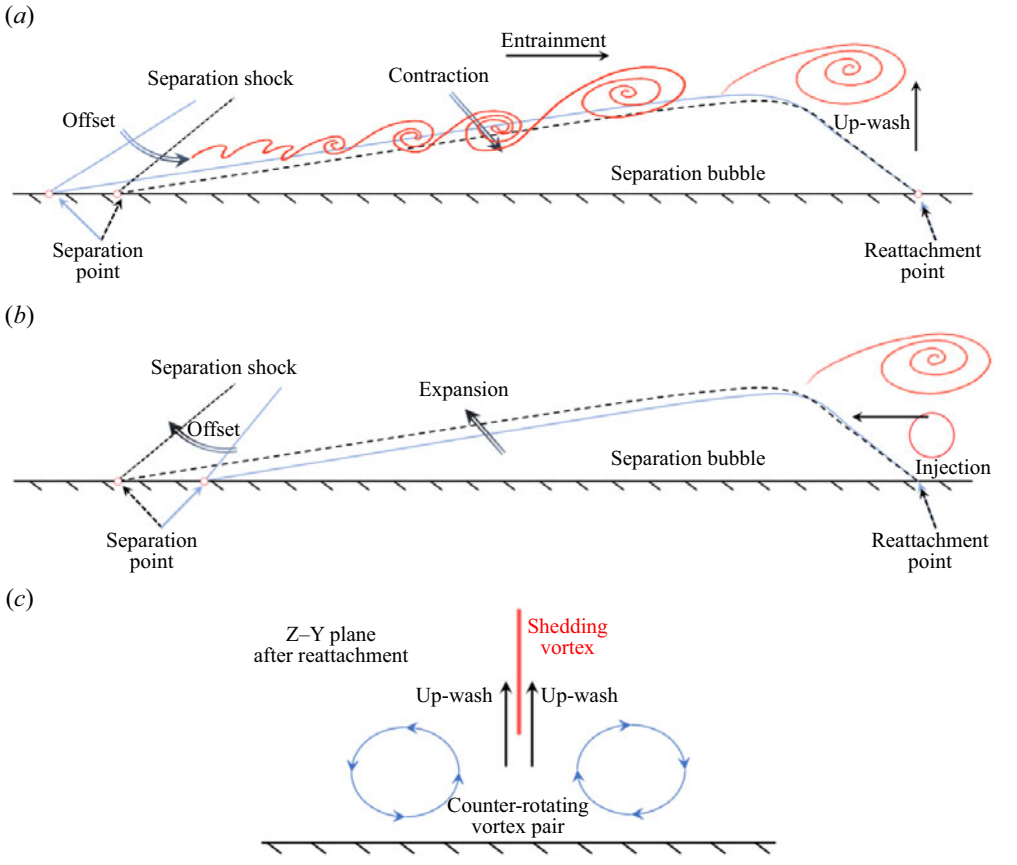

Figure 39. Sketch of the entrainment–injection model sustained by the CVP: (*a*) contraction process, (*b*) dilatation process and (*c*) schematic diagram for up-wash effect of the shedding vortex. The black dashed and blue solid lines signify the flow structure in the averaged flow field and instantaneous flow field.

pattern. In canonical cases including impinging shock and ramp cases, the entrainment usually only occurs in the rear half of the separation bubble, leading to a non-dimensional entrainment length $X_r^{ent} \approx 0.5$ (Piponniau *et al.* 2009). For the unstart flow of the REST inlet, the instability is affected by the CLE shock at the maximum thickness of the separation bubble. Therefore, the entrainment only occurs after the impinging point of the CLE shock, resulting in an approximate non-dimensional entrainment length $X_r^{ent} \approx 0.15$ and the geometry-dependent transformation factor is $C^{ent} = (X_r^{ent})^2 L_r/h \approx 7.7$. The entrainment frequencies St_r^{ent} of these cases are similar, thus the REST inlet unstart flow yields an approximately 5 times larger St_r^{ent} than the impinging shock and ramp cases, and 2.5 times larger St_r^{ent} than the forward- and backward-facing step cases under the same free-stream condition. However, this model only provides an estimate of the low frequency, and an accurate value is not expected to be obtained.

Based on the discussion above, the following physical mechanism is proposed for the low-frequency unsteadiness in the REST inlet unstart flow. The incoming flow undergoes a strong adverse pressure gradient and shear upon separation, leading to large coherent vortical structures along the shear layer. Near the maximum thickness location of the bubble, the shear layer rapidly becomes unstable, which is affected by the CLE shock. correspondingly, the shedding vortices are formed and the mass is entrained as displayed

in figure 39(*a*). Moreover, the streamwise vortices are generated around the reattachment driven by the shedding vortices and centrifugal instability. Under the joint effect of shedding vortices and large-scale streamwise vortices, the mass is injected into the separation bubble, thus the scale and the location of the separation bubble are sustained. Additionally, the consecutive entrainment recharge leads to the breathing of the separation bubble as well as the flapping of the separation shock, as observed from the streamwise velocity fluctuations of the DMD mode in figures 33–37. Therefore, the large-scale vortices and the shedding vortices are the main driving force of the global low-frequency unsteadiness of the REST inlet unstart flow under the off-design condition.

5. Conclusions

Numerical simulation was carried out by DDES to study the unsteady mechanism of the REST inlet unstart flow under the off-design condition at a Mach of 4. With the help of highly accurate numerical simulations, the mechanism of unsteadiness, especially the low-frequency characteristics, is investigated. Compared with the canonical SWBLI cases, the flow topology of the REST inlet unstart flow shows significantly different features since the REST inlet consists of irregular compression surfaces generated by a comprehensive consideration of streamline tracking and shape transition rather than the multiple ramps in the two-dimensional inlet. In the REST inlet unstart flow under the off-design condition, a large-scale separation bubble is located on the compression surfaces with a separation shock in front of the bubble. Near the maximum thickness of the bubble, a CLE shock induced by the CLE interacts with the shear layer and accelerates the instability of the shear layer. Moreover, strong unsteady motion can be observed in the unstart flow, including the breathing of the separation bubble, flapping of the separation shock, interaction between the CLE shock and shear layer, instability of the shear layer and the generation of the shedding vortices. Among them, the most unstable global motion is distributed around the shear layer and the region where the shedding vortex forms.

From the spectral analysis, there is a broad band of low-frequency oscillations in the REST inlet unstart flow. The lower-frequency dynamics is associated with the breathing of the separation bubble and the flapping motion of the separation shock wave, while the higher frequency is related to the instability of the shear layer affected by the CLE shock and the formation of shedding vortices. The phenomena mentioned below have a significant influence on the flow capture characteristic of the unstart inlets. Further, coherence analysis shows that the contributions of these flow structures dominating the low-frequency dynamics are coupling with each other. For this, three-dimensional DMD analysis is carried out to reveal the characteristics that contribute to the observed unsteady behaviour. The large fluctuations observed in mode ϕ_1 illustrate that the separation bubble and separation shock are the most significant flow patterns for the REST inlet unstart flow, as can be seen in figure 21. Mode ϕ_2 provides evidence that low-frequency motion is associated with the breathing of the shock waves and shear layer. Mode ϕ_3 with higher dominant frequency is related to the motion of shedding vortices. At the same time, the elongated distributed streamwise velocity fluctuations indicate that the generation of the streamwise structures around the reattachment is coupled with the motion of shedding vortices. The streamwise vortices and the shedding vortices are the main driving force of the global low-frequency unsteadiness of the REST inlet unstart flow under the off-design condition. Moreover, the CLE shock plays an important role in the process during the dominant flow structure conversion from the backflow within the separated region into the elongated streamwise structure.

Funding. This study was co-supported by National Natural Science Foundation of China (no. 11902265, no. 11972308) and Natural Science Foundation of Shaanxi Province (no. 2019JQ-376) and the Fundamental Research Funds for the Central Universities (no. G2018KY0304, no. G2018KY0308).

Declaration of interests. The authors report no conflict of interest.

Data availability statement. The data that support the findings of this study are available from the corresponding author upon reasonable request.

Author ORCIDs.
Jiaxiang Zhong https://orcid.org/0000-0001-8619-208X;
Feng Qu https://orcid.org/0000-0001-8811-0674;
Qing Wang https://orcid.org/0000-0002-5769-5451.

References

Bagheri, H., Mirjalily, S.A.A., Oloomi, S.A.A. & Salimpour, M.R. 2021 Effects of micro-vortex generators on shock wave structure in a low aspect ratio duct, numerical investigation. *Acta Astronaut.* **178**, 616–624.

Bogdanoff, D.W. 1983 Compressibility effects in turbulent shear layers. *AIAA J.* **21** (6), 926–927.

Chang, J., Li, N., Xu, K., Bao, W. & Yu, D. 2017 Recent research progress on unstart mechanism, detection and control of hypersonic inlet. *Prog. Aerosp. Sci.* **89**, 1–22.

Chen, H. & Tan, H.-j. 2019 Buzz flow diversity in a supersonic inlet ingesting strong shear layers. *Aerosp. Sci. Technol.* **95**, 105471.

Devaraj, M.K.K., Jutur, P., Rao, S.M.V., Jagadeesh, G. & Anavardham, G.T.K. 2021 Investigation of local unstart in a hypersonic scramjet intake at a Mach number of 6. *Aerosp. Sci. Technol.* **115**, 106789.

Estruch-Samper, D. & Chandola, G. 2018 Separated shear layer effect on shock-wave/turbulent-boundary-layer interaction unsteadiness. *J. Fluid Mech.* **848**, 154–192.

Fu, L., Bose, S. & Moin, P. 2022 Prediction of aerothermal characteristics of a generic hypersonic inlet flow. *Theor. Comput. Fluid Dyn.* **36** (2), 345–368.

Ganapathisubramani, B., Clemens, N.T. & Dolling, D.S. 2007 Effects of upstream boundary layer on the unsteadiness of shock-induced separation. *J. Fluid Mech.* **585**, 369–394.

Grilli, M., Hickel, S. & Adams, N.A. 2013 Large-eddy simulation of a supersonic turbulent boundary layer over a compression–expansion ramp. *Intl J. Heat Fluid Flow* **42**, 79–93.

Hillier, R. 2007 Shock-wave/expansion-wave interactions and the transition between regular and Mach reflection. *J. Fluid Mech.* **575**, 399–424.

Hu, W., Hickel, S. & Van Oudheusden, B. 2019 Dynamics of a supersonic transitional flow over a backward-facing step. *Phys. Rev. Fluids* **4** (10), 103904.

Hu, W., Hickel, S. & Van Oudheusden, B. 2020 Influence of upstream disturbances on the primary and secondary instabilities in a supersonic separated flow over a backward-facing step. *Phys. Fluids* **32**, 056102.

Hu, W., Hickel, S. & Van Oudheusden, B.W. 2021 Low-frequency unsteadiness mechanisms in shock wave/turbulent boundary layer interactions over a backward-facing step. *J. Fluid Mech.* **915**, A107.

Huang, H.-x., Tan, H.-j., Sun, S. & Wang, Z.-y. 2018 Behavior of shock train in curved isolators with complex background waves. *AIAA J.* **56** (1), 329–341.

Im, S.-k. & Do, H. 2018 Unstart phenomena induced by flow choking in scramjet inlet-isolators. *Prog. Aerosp. Sci.* **97**, 1–21.

Jin, Y., Zhang, Y., Tan, H.-J., Li, X., Sun, S. & Wang, D.-P. 2022 Oscillations in rectangular supersonic inlets with large internal contraction ratio. *AIAA J.* **60** (8), 4628–4638.

Johnson, E., Jenquin, C., McCready, J., Narayanaswamy, V. & Edwards, J. 2023 Experimental investigations of the hypersonic stream-traced performance inlet at subdesign Mach number. *AIAA J.* **61** (1), 23–36.

Kussoy, M.I. & Horstman, K.C. 1992 Intersecting shock-wave/turbulent boundary-layer interactions at Mach 8.3. *NASA Tech. Rep. TM-103909*.

Lewis, M. 2010 X-51 scrams into the future. *Aerosp. Am.* **48** (9), 27–31.

Li, N., Chang, J., Jiang, C., Yu, D., Bao, W., Song, Y. & Jiao, X. 2018 Unstart/restart hysteresis characteristics analysis of an over–under TBCC inlet caused by backpressure and splitter. *Aerosp. Sci. Technol.* **72**, 418–425.

LI, N., CHANG, J., YU, D., BAO, W. & SONG, Y. 2017 Mathematical model of shock-train path with complex background waves. *J. Propul. Power* **33** (2), 468–478.

LIU, X., LIANG, J. & WANG, Y. 2016 Flow mechanism in a hypersonic sidewall compression inlet with a rectangular-to-circular isolator. *J. Spacecr. Rockets* **53** (3), 549–557.

LIU, X.-D., OSHER, S. & CHAN, T. 1994 Weighted essentially non-oscillatory schemes. *J. Comput. Phys.* **115** (1), 200–212.

MENTER, F.R. 1994 Two-equation eddy-viscosity turbulence models for engineering applications. *AIAA J.* **32** (8), 1598–1605.

PAPAMOSCHOU, D. & ROSHKO, A. 1988 The compressible turbulent shear layer: an experimental study. *J. Fluid Mech.* **197**, 453–477.

PASQUARIELLO, V., HICKEL, S. & ADAMS, N.A. 2017 Unsteady effects of strong shock-wave/boundary-layer interaction at high Reynolds number. *J. Fluid Mech.* **823**, 617–657.

PIPONNIAU, S., DUSSAUGE, J.-P., DEBIEVE, J.-F., & DUPONT, P. 2009 A simple model for low-frequency unsteadiness in shock-induced separation. *J. Fluid Mech.* **629**, 87–108.

QIN, B., CHANG, J., JIAO, X. & BAO, W. 2015 Unstart margin characterization method of scramjet considering isolator–combustor interactions. *AIAA J.* **53** (2), 493–500.

QU, F., CHEN, J., SUN, D., BAI, J. & ZUO, G. 2019 A grid strategy for predicting the space plane's hypersonic aerodynamic heating loads. *Aerosp. Sci. Technol.* **86**, 659–670.

QU, F. & SUN, D. 2017 Investigation into the influences of the low-speed flows' accuracy on RANS simulations. *Aerosp. Sci. Technol.* **70**, 578–589.

RODRIGUEZ, C.G. 2003 Computational fluid dynamics analysis of the central institute of aviation motors/NASA scramjet. *J. Propul. Power* **19** (4), 547–555.

ROHDE, J. 1992 Airbreathing combined cycle engine systems. In *Rocket-Based Combined-Cycle (RBCC) Propulsion Technology Workshop. Tutorial Session*.

ROWLEY, C.W., MEZIĆ, I., BAGHERI, S., SCHLATTER, P. & HENNINGSON, D.S. 2009 Spectral analysis of nonlinear flows. *J. Fluid Mech.* **641**, 115–127.

SAKATA, K., YANAGI, R., MURAKAMI, A., SHINDO, S., HONAMI, S., SHIZAWA, T., SAKAMOTO, K., SHIRAISHI, K. & OMI, J. 1993 An experimental study of supersonic air-intake with 5-shock system at Mach 3. In *AIAA, SAE, ASME, and ASEE, Joint Propulsion Conference and Exhibit, 29th, Monterey, CA*, p. 1993.

SANDHAM, N.D. & REYNOLDS, W.C. 1990 Compressible mixing layer-linear theory and direct simulation. *AIAA J.* **28** (4), 618–624.

SCHMID, P.J. 2010 Dynamic mode decomposition of numerical and experimental data. *J. Fluid Mech.* **656**, 5–28.

SEGAL, C. 2009 *The Scramjet Engine: Processes and Characteristics*, vol. 25. Cambridge University Press.

SETHURAMAN, V.R.P., KIM, T.H. & KIM, H.D. 2021 Effects of back pressure perturbation on shock train oscillations in a rectangular duct. *Acta Astronaut.* **179**, 525–535.

SMART, M.K. 1999 Design of three-dimensional hypersonic inlets with rectangular-to-elliptical shape transition. *J. Propul. Power* **15** (3), 408–416.

SMART, M.K. & TREXLER, C.A. 2004 Mach 4 performance of hypersonic inlet with rectangular-to-elliptical shape transition. *J. Propul. Power* **20** (2), 288–293.

SPALART, P.R., DECK, S., SHUR, M.L., SQUIRES, K.D., STRELETS, M.KH. & TRAVIN, A. 2006 A new version of detached-eddy simulation, resistant to ambiguous grid densities. *Theor. Comput. Fluid Dyn.* **20**, 181–195.

SUN, D., QU, F., LIU, C., YAO, F. & BAI, J. 2021 Numerical study of the suction flow control of the supersonic boundary layer transition in a framework of gas-kinetic scheme. *Aerosp. Sci. Technol.* **109**, 106397.

SUN, D., QU, F. & YAN, C. 2018 An effective flux scheme for hypersonic heating prediction of re-entry vehicles. *Comput. Fluids* **176**, 109–116.

TAN, H.J., SUN, S. & HUANG, H.X. 2012 Behavior of shock trains in a hypersonic inlet/isolator model with complex background waves. *Exp. Fluids* **53**, 1647–1661.

TAN, H.-J., LI, L.-G., WEN, Y.-F. & ZHANG, Q.-F. 2011 Experimental investigation of the unstart process of a generic hypersonic inlet. *AIAA J.* **49** (2), 279–288.

TAN, H.-J., SUN, S. & YIN, Z.-L. 2009 Oscillatory flows of rectangular hypersonic inlet unstart caused by downstream mass-flow choking. *J. Propul. Power* **25** (1), 138–147.

TOUBER, E. & SANDHAM, N.D. 2009 Large-eddy simulation of low-frequency unsteadiness in a turbulent shock-induced separation bubble. *Theor. Comput. Fluid Dyn.* **23**, 79–107.

TOUBER, E. & SANDHAM, N.D. 2011 Low-order stochastic modelling of low-frequency motions in reflected shock-wave/boundary-layer interactions. *J. Fluid Mech.* **671**, 417–465.

TRAPIER, S., DECK, S. & DUVEAU, PH. 2008 Delayed detached-eddy simulation and analysis of supersonic inlet buzz. *AIAA J.* **46** (1), 118–131.

VOLAND, R., AUSLENDER, A., SMART, M., ROUDAKOV, A., SEMENOV, V. & KOPCHENOV, V. 1999 CIAM/NASA Mach 6.5 scramjet flight and ground test. In *9th International Space Planes and Hypersonic Systems and Technologies Conference*, p. 4848.

WANG, D., LI, Z., ZHANG, Z., LIU, N.-S., YANG, J. & LU, X.-Y. 2018 Unsteady shock interactions on V-shaped blunt leading edges. *Phys. Fluids* **30** (11), 116104.

WANG, Q., QU, F., SUN, D. & BAI, J. 2023 Numerical study of instabilities and compressibility effects on supersonic jet over a convex wall. *J. Fluid Mech.* **954**, A6.

WANG, Q., QU, F., ZHAO, Q. & BAI, J. 2022 Numerical study of the hysteresis effect on the supercritical airfoil for the transonic circulation control. *Aerosp. Sci. Technol.* **126**, 107645.

XU, K., CHANG, J., ZHOU, W. & YU, D. 2016 Mechanism and prediction for occurrence of shock-train sharp forward movement. *AIAA J.* **54** (4), 1403–1412.

YIMING, L., ZHUFEI, L. & ZHANG, Y. 2021 Tomography-like flow visualization of a hypersonic inward-turning inlet. *Chinese J. Aeronaut.* **34**, 44–49.

YU, K., XU, J., LI, R., LIU, S. & ZHANG, X. 2018 Experimental exploration of inlet start process in continuously variable Mach number wind tunnel. *Aerosp. Sci. Technol.* **79**, 75–84.

YUAN, H. & LIANG, D.-W. 2006 Analysis of characteristics of restart performance for a hypersonic inlet. *J. Propul. Technol.-Beijing* **27** (5), 390.

ZHANG, Z., LI, Z. & YANG, J. 2021 Transitions of shock interactions on V-shaped blunt leading edges. *J. Fluid Mech.* **912**, A12.

ZHENG, Y., YAN, C. & ZHAO, Y. 2020 Uncertainty and sensitivity analysis of inflow parameters for HyShot II scramjet numerical simulaiton. *Acta Astronaut.* **170**, 342–353.

ZHONG, J., QU, F., SUN, D., FU, J., WANG, X., WANG, Z. & BAI, J. 2023 Numerical investigation of the unstart flow at off-design condition of rest inlet at a Mach of 4. *Aerosp. Sci. Technol.* **136**, 108232.

ZVEGINTSEV, V.I. 2017 Gas-dynamic problems in off-design operation of supersonic inlets. *Thermophys. Aeromech.* **24**, 807–834.